

**MODIS Clear Water Epsilons
Algorithm Theoretical Basis Document**

ATBD 21

**Version 6
June 2002**

Kendall L. Carder, Christopher Catrall, F. Robert Chen

**College of Marine Science
University of South Florida
140 Seventh Avenue South
St. Petersburg, FL 33701 USA**

Preface

This document describes the present state of development of the algorithm for detecting the presence of mineral dust aerosols in remote sensing imagery. Recent results from the University of South Florida and NASA-Goddard Space Flight Center demonstrate that mineral dust absorbs moderately in the blue wavelengths, but negligibly in the green, red and near infrared (NIR) wavelengths, contrary to previous beliefs that mineral dust absorption was non-negligible throughout the visible and NIR. Since current atmospheric correction algorithms depend on the red and NIR to deduce the aerosol type present in the image, mineral dust is undetectable by current atmospheric correction algorithms. The clear-water epsilon approach uses information at all wavelengths (MODIS or SeaWiFS), and known reflectance characteristics of low chlorophyll ($[chl\ a] < 0.5\ mg/m^3$) waters to deduce the presence of blue-absorbing mineral dust. In previous versions of this algorithm, mineral dust absorption was assumed detectable in the mid-visible wavelengths (520, 550 nm), but with these new results, this approach would be nearly as insensitive as current atmospheric correction algorithms to the presence of mineral dust. Absorption in the blue and ultraviolet wavelengths is detectable, however, and it is this fact that has allowed progress in developing a flag for mineral dust. In this ATBD version 6, we present recent work on characterizing the optical properties of African mineral dust and a new method to detect the presence of mineral dust in remote sensing images.

1.0 Introduction

Observations from space cannot furnish the complete set of aerosol radiative parameters [Tanré *et al.*, 1996], and remote sensing of both aerosol and Earth's ecosystems depend on aerosol models to determine many surface and atmospheric properties [Gordon, 1997; Kahn *et al.*, 1998; Kaufman *et al.*, 2001; Mishchenko *et al.*, 1999; Torres *et al.*, 1998; Vermote *et al.*, 1997]. This is particularly true for remote sensing over the ocean, where surface and atmospheric effects dominate the light received at the sensor and models are used exclusively to predict and remove the contaminant signal from the water-leaving radiance at shorter wavelengths [Gordon, 1997]. The aerosol radiance at the NIR wavelengths is rather insensitive to differences in aerosol chemical composition, however, and the presence of absorbing aerosols (e.g., mineral dust, soot) causes unacceptable error in the atmospheric correction algorithm [Gordon, 1997]. This effect has been observed in both CZCS [Carder *et al.*, 1991; Fukushima and Toratami, 1997] and SeaWiFS [Gordon *et al.*, 2000] imagery. The simultaneous solution of water-leaving radiance and atmospheric optical properties holds promise for dealing with absorbing aerosols [Moulin *et al.*, 2001b], but the aerosol models used in the retrieval must still accurately represent those found in nature.

Iron, an essential nutrient for phytoplankton, is believed to limit oceanic productivity in areas where the supply of nitrogen, phosphorus and silicon far exceeds demand [Martin and Gordon, 1988; Martin *et al.*, 1991]. Mesoscale iron fertilization experiments have shown increases in phytoplankton productivity, biomass, and chlorophyll in the equatorial Pacific and Southern Ocean [Boyd *et al.*, 2000; Coale *et al.*, 1996]. These regions, as well as the North Pacific, are described as high-nitrate low-chlorophyll (HNLC) areas and believed to display iron limitation. Aeolian mineral dust is the dominant source of iron to much of the remote ocean [Duce and Tindale, 1991]; a natural conclusion follows that dissolution of iron-bearing dust could stimulate phytoplankton growth in HNLC regions [Martin, 1990]. Indeed, increased primary productivity has been observed in the North Pacific following dust deposition [Young

et al., 1991]. Further fueling the debate over iron fertilization is the clear relationship between concentrations of mineral dust and atmospheric carbon dioxide (a proxy for primary production) in ice core samples [*Petit et al.*, 1999]. Consequently, much work has focussed on modelling dust flux to the ocean [*Gao et al.*, 2001; *Mahowald et al.*, 1999; *Tegen and Fung*, 1994] and the oceanic iron cycle [*Archer and Johnson*, 2000; *Fung et al.*, 2000].

The primary purpose of this algorithm is to contrast a measured epsilon value, $\epsilon(531,667)$, over clear waters to estimate the presence of iron in the aerosol content. In addition, for regions where $\epsilon(531,667)$ is significantly less than $\epsilon(750,865)$, the standard MODIS $L_{wn}(\lambda)$ values at shorter wavelengths will be suspect due to the blue-absorbing aerosols. Thus, a second purpose of this algorithm is to recalculate such suspect $L_{wn}(\lambda)$ values using the clear-water epsilon technique. Last, since these effects will not be discernible from Angström exponents derived using ratios of longer wavelengths, $\epsilon(531,667)$ can also provide a check on the Angström exponent derived at red and infra-red wavelengths.

The method for obtaining clear-water epsilon values (Gordon and Clark, 1981; Gordon et al., 1983) have been thoroughly documented in the CZCS literature. No significant alterations to this earlier approach have been applied other than the extension of the clear water concept to include waters with higher pigment concentrations. We did modify the values of the normalized water-leaving radiance at 520, 550, and 670 nm for CZCS to the slightly different MODIS bands by means of the water absorption curve.

2.0 Overview and Background Information

One goal of MODIS is the determination of the chlorophyll pigment concentration within a 35% error. This ability rests squarely upon the accuracy of the water-leaving radiance retrievals. The strong absorption of blue light by dust aerosols will seriously undermine this effort if not detected.

2.1 Experimental Objectives

The objectives of this experiment are two-fold: 1) to provide a means of identifying blue-absorbing aerosols over clear waters and to estimate the iron flux to the ocean via these aerosols, and 2) to flag instances when L_{wn} retrievals may need adjustment due to aerosol absorption at blue and green wavelengths. Such errors will affect calculations of $[chl\ a]$ using MODIS.

2.2 Historical Perspective

The success of the CZCS atmospheric correction algorithm in estimating and removing atmospheric effects is evident from its ability to determine the water-leaving radiance within about 10% for much of the world oceans, and chlorophyll concentrations to within approximately 40% under optimal conditions [Gordon *et al.*, 1983]. The flurry of research initiated by the success of the CZCS and improved remote sensing technology have led to vastly increased expectations and greater hopes for the next generation of ocean-viewing color sensors. MODIS will have a better radiometric sensitivity than CZCS due to a larger signal-to-noise ratio and a 12-bit digitization as compared with the 8-bit CZCS. This has necessitated the consideration of the full complexities of multiple scattering, oceanic whitecaps, earth curvature, and improved aerosol modeling [Gordon and Wang, 1992a; Gordon and Wang, 1994a].

2.3 Instrument Characteristics

The MODIS radiometric specifications are included in Table 1, after [Gordon, 1994]. The noise equivalent reflectance ($NE\Delta\rho$) is derived using a solar angle of 60° and taken at the scan edge in order to

Band	Bandwidth [center]	$\rho_i(\text{sr}^{-1}) (\theta_o = 60^\circ)$	$NE\Delta L (\text{sr}^{-1})$	$NE\Delta\rho (\text{sr}^{-1})$	Required SNR
8	405-420 [412]	0.34	0.000052	0.00018	880
9	438-448 [443]	0.29	0.000050	0.00016	838
10	483-493 [490]	0.23	0.000043	0.00014	802
11	526-536 [531]	0.19	0.000041	0.00013	754
12	546-556 [551]	0.154	0.000030	0.00010	750
13	662-672 [667]	0.105	0.0000097	0.00004	910
14	673-683 [681]	0.105	0.0000094	0.00004	1087
15	743-753 [750]	0.081	0.000017	0.000085	586
16	862-877 [865]	0.069	0.000012	0.000076	516

simulate the least favorable viewing geometry. In addition to CZCS channels, MODIS has been equipped with a 412 nm band for separating the detrital and viable phytoplankton signals, and two bands centered on 750 and 865 nm to aid in atmospheric correction. To recover the normalized water-leaving reflectance in the blue to within $< 5\%$ requires the accuracy of atmospheric correction to be within $\pm 0.001 - 0.002$ in reflectance at 443 nm [Gordon, 1996].

3.0 Algorithm Development and Description

An introduction to both the historical and recent methods of atmospheric correction are required in order to appreciate the meaning of the spectral behaviour of absorption of dust aerosols. Thus, CZCS and MODIS correction schemes will be briefly touched upon before discussing aerosol absorption. Our notation duplicates that of ATBD MOD18, where a complete description of the theory and nomenclature may be obtained. The single-scattering approximation will be used here until a reliable optical model for mineral dust has been determined which may then be used as input to our radiative transfer code to effect the full multiple scattering solution.

3.1 Physics of the Problem

Up to 90% of the total radiance received at the sensor for most cloud-free scenes is due to the intervening atmosphere (Gordon et al., 1983). Aerosol scattering may be responsible for 10 to 40% of the radiance. Scattering by aerosols thus represents an important optical component of the atmosphere which must be removed from MODIS imagery before water-leaving radiances, hence chlorophyll, can be determined. Furthermore, aerosol concentrations and optical characteristics vary in both time and space. Thus the contribution of backscattered radiance by aerosols to the total radiance observed by the sensor cannot be estimated and removed *a priori*, as can the contribution by Rayleigh scattering.

Essentially, the single-component atmospheric correction algorithm rests on quasi-single scattering theory and the clear water radiance technique (Gordon and Clark, 1981; Gordon et al., 1983). Single scattering theory allows Rayleigh scattering radiance (L_r), aerosol scattering radiance (L_a), and water-leaving radiance (L_w) to be separated. The clear-water radiance technique utilizes *a priori* knowledge of the water-leaving radiance of low-chlorophyll sea water at 531, 551, and 667 nm to calculate the

contribution of aerosol scattering to the total radiance received at the sensor (L_t) at each of the wavelengths. The water-leaving radiance at 443 nm (the band most sensitive to chlorophyll absorption) is then determined through extrapolation of the aerosol radiance to 443 nm. Treatment of the Rayleigh and aerosol scattering in a single scattering sense (i.e., as independent terms) results in errors in aerosol radiance values less than 10% for aerosol optical thicknesses (τ_a) less than 0.6 under most conditions with non-absorbing aerosols (Gordon et al., 1983).

3.2 Atmospheric Correction

Radiance resulting from scattering is denoted in the literature by $L_x(\lambda)$, x representing the source of the scattered signal, such as Rayleigh (r), aerosol (a), or multiple (ar , ra) scattering. It is more convenient and physically meaningful to use *reflectance* [Gordon and Clark, 1981] (θ_o representing the solar zenith angle and F_0 the extraterrestrial solar irradiance),

$$\rho_x(\lambda) = \frac{\pi}{F_o(\lambda) \cdot \cos \theta_o} L_x(\lambda)$$

The complete formulation of the correction algorithms have been thoroughly documented [Gordon et al., 1988; Gordon and Clark, 1981; Gordon and Wang, 1994b] and shall not be reviewed here. The quantity of importance is the ratio of aerosol reflectances (denoted by as) received by the sensor at wavelengths λ_i and λ_j and a viewing angle θ_v :

$$\varepsilon(\lambda_i, \lambda_j) \equiv \frac{\rho_{as}(\lambda_i)}{\rho_{as}(\lambda_j)} = \frac{\omega_a(\lambda_i) \cdot \tau_a(\lambda_i) \cdot p_a(\theta_v, \phi_v; \theta_o, \phi_o; \lambda_i)}{\omega_a(\lambda_j) \cdot \tau_a(\lambda_j) \cdot p_a(\theta_v, \phi_v; \theta_o, \phi_o; \lambda_j)}$$

The parameters $\tau_a(\lambda)$, $\omega_a(\lambda)$, and p_a are, respectively, the aerosol optical thickness, single-scattering albedo, and aerosol scattering phase function. Physically, $\varepsilon(\lambda_i, \lambda_j)$ represents the relative strengths of the aerosol scattering and absorption, largely independent of the power of the light incident upon the aerosol particles, viewing geometry, and the concentration of aerosol particles present.

For large, iron-rich, desert dust particles, the ratio of aerosol reflectances at 550 nm and 670 nm, $\epsilon(550, 670)$, has been shown using CZCS data to decrease to 0.94 and below [Carder *et al.*, 1991] during strong dust events; typical values of 1.0-1.5 are found for smaller, non-iron-bearing aerosols. In such occurrences, when aerosol reflectance is lower in the blue than the green or red, strong absorption is likely present.

Assuming complete avoidance of sun glitter, the total reflectance received at an ocean-viewing sensor can be described by:

$$\rho_t(\lambda) = \rho_r(\lambda) + \rho_a(\lambda) + \rho_{ra}(\lambda) + t(\lambda) \cdot [\rho_{wc}(\lambda) + \rho_w(\lambda)], \text{ where}$$

$$t(\lambda) = e^{-(\tau_R(\lambda)/2 + \tau_{oz}(\lambda) + (1 - \omega_{as}(\lambda) \cdot F) \tau_{as}(\lambda)) / \cos \theta_o}$$

The subscripts represent the contributions from Rayleigh scattering, aerosol interactions (absorption *and* scattering), Rayleigh-aerosol interactions, whitecaps, and water-leaving radiance, respectively, and F the probability of forward scattering. Rayleigh scattering and whitecap reflectance may be determined *a priori* with knowledge of sun and spacecraft zenith angles and wind velocity. The diffuse transmittance of the atmosphere, $t(\lambda)$, is considered known since it is primarily a function of Rayleigh and ozone optical thickness (τ_r and τ_{oz}) and the satellite zenith viewing angle, θ_o , and only secondarily a function of aerosol attenuation [Gordon *et al.*, 1983]. Thus, separation of the total signal into components is reduced to that of determining the aerosol and water-leaving radiances.

3.2.1 CZCS

Separation of $\rho_w(\lambda)$ and $\rho_{as}(\lambda)$ was effected for the CZCS using quasi-single scattering theory and clear-water radiances [Gordon and Clark, 1981]. The basis for this theory is that where chlorophyll *a* plus pheophytin *a* concentrations (C) are less than 0.25 mg m⁻³, the normalized water-leaving radiances,

$L_{wn}(\lambda_i)$ can be designated *a priori* to within 10%. At 520, 550, and 670 nm these values are 0.495, 0.28, and less than $0.015 \text{ mW cm}^{-2} \mu\text{m}^{-1} \text{ sr}^{-1}$, respectively. Thus, $\epsilon(520,670)$ and $\epsilon(550,670)$ were determined over clear water. For a given wavelength, $L_w(\lambda_i)$ can be related to $L_{wn}(\lambda_i)$ through

$$L_w(\lambda_i) = L_{wn}(\lambda_i)t(\theta_o, \lambda_i)\cos\theta_o$$

Clear-water radiances now determine $\rho_w(520)$, $\rho_w(550)$ and $\rho_w(670)$, yielding $\rho_{as}(\lambda)$ for these wavelengths at each pixel in a clear-water region (presumed to include most ocean regions away from land and within 35° latitude from the equator). Using the assumption that the aerosol size distribution behaved according to [Junge, 1963],

$$\frac{dn(a)}{da} = C(z) \cdot a^\gamma,$$

where n is the aerosol particle number density, a the particle radius and γ the Junge parameter, the aerosol optical depth is given by [Gregg and Carder, 1990; van de Hulst, 1957]:

$$\begin{aligned}\tau_a(\lambda) &= K \cdot \lambda^{-(\gamma+3)} \\ &= K \cdot \lambda^{-\eta_\tau(\lambda)}, \quad \eta_\tau = \gamma + 3 \text{ (Angström exponent)}\end{aligned}$$

A further assumption of a single scattering albedo of unity and non-spectral phase functions gives the aerosol epsilon:

$$\epsilon(\lambda_i, \lambda_j) = \frac{\rho_{as}(\lambda_i)}{\rho_{as}(\lambda_j)} = \left(\frac{\lambda_i}{\lambda_j}\right)^{-\eta_\tau(\lambda_i)}$$

The epsilon values $\epsilon(\lambda_i, 670)$ derived for CZCS spectral bands 2, 3, and 4 were spatially averaged and used to "type" the aerosol by determining an average Angström exponent, allowing $\epsilon(443, 670)$ to be determined. This method is usually applied to a 5-by-5 pixel region of a clear water portion of the scene to increase the signal-to-noise ratio. $\rho_w(443)$ is then determined by,

$$\rho_w(443) = \frac{1}{t(\lambda)} [\rho_i(443) - \rho_r(443) - \epsilon(443, 670) \cdot \rho_{as}(670)]$$

Treatment of the Rayleigh and aerosol scattering in a single-scattering manner results in errors in aerosol radiance values less than 10% for aerosol optical thickness (τ_a) less than 0.6, under most conditions [Gordon *et al.*, 1983].

3.2.2 MODIS

While the Angström formulation was sufficiently accurate from 520-670 nm, the CZCS wavelength range, Monte Carlo simulations using published values of aerosol size distributions and refractive indices [Shettle and Fenn, 1979] at varying wavelengths, scan geometries, and relative humidities have shown that over the MODIS range 531-865 nm this formulation was a poor approximation [Gordon, 1996]. Gordon's results suggest

$$\varepsilon(\lambda_i, \lambda_j) = e^{c(\lambda_j - \lambda_i)},$$

where c is a constant depending on aerosol model and relative humidity, would be a more accurate parametrization of the problem.

Aerosol reflectance may be obtained over clear water at 750 and 865 nm since the water-leaving radiances are zero, providing a determination of the constant c . This parametrizes the aerosol reflectances over all wavelengths. Note this stems purely from the signals received at 750 and 865 nm, an area of the spectrum normally exhibiting negligible absorption by iron-rich mineral aerosols. An aerosol with optical signatures exhibiting differing spectral dependence will confound this method further than the CZCS approach, which uses visible channels in the atmospheric correction.

3.3 Clear-water epsilons and aerosol absorption

Mineral dust absorbs in the blue and ultraviolet wavelengths due to iron oxide impurities [Claquin *et al.*, 1999; Sokolik and Toon, 1999]. A consensus on the magnitude of the absorption has proved

elusive, with laboratory measurements placing ω_0 at 0.5 μm between 0.63 and 0.87 [see *Sokolik and Toon*, 1996] and broadband flux measurements placing ω_0 at 0.95 [*Fouquart et al.*, 1986]. The former values are several times greater than recent computations using constituent optical properties [*Sokolik and Toon*, 1999] and disparate remote sensing techniques [*Dubovik et al.*, 2002; *Kaufman et al.*, 2001; *Tanré et al.*, 2001](see Appendix B, Fig. B14). The limited number of wavelengths in these retrievals, however, prevents the spectral behaviour of mineral dust absorption across the visible and near infrared from being known. To determine the spectral behaviour of absorption by mineral dust, we developed a sensitive hyperspectral method for determining the single-scattering albedo and phase function of mineral dust from ground-based sky radiance and optical depth measurements (see Appendix B). These values will soon be used to construct look-up tables for at-sensor radiance. As recent results indicate a lack of absorption at wavelengths above 500 nm, a knowledge of $\epsilon(531,667)$, $\epsilon(551, 667)$ will likely not be enough to flag absorbing aerosols. We have developed a further test that is sensitive specifically to absorption by aerosols in the blue wavelengths of ocean colour sensors.

3.3.1 Use of 412 and 443 nm to detect light absorption by mineral dust. An important tool for evaluating field and satellite data sets of water-leaving radiance was developed for waters where chlorophyll-like pigments are less than 0.25 mg m⁻³ [Gordon, 1981]. The value of this tool is that it provides a means of predicting what values the normalized water-leaving radiance, $nL_w(\lambda)$, should have for $\lambda \geq 520$ nm in the subtropical central gyres of the ocean. The clear-water $nL_w(\lambda)$ values for the CZCS for 520, 550, and 670 nm are 0.495, 0.280, and <0.015 mW cm⁻² um⁻¹ sr⁻¹, respectively [Gordon, 1983]. Dividing $nL_w(\lambda)$ by extraterrestrial values of solar irradiance, $F_o(\lambda)$, gives the remote-sensing reflectance, $R_{rs}(\lambda)$. At 550 nm, the clear-water R_{rs} value becomes approximately 0.0015 sr⁻¹. Values straying from the expected clear-water radiances suggest problems in sensor calibration or atmospheric correction. If the problem persists over a variety of days or geographical locations, then in the fault most likely is one of instrument calibration.

A somewhat similar approach has been used to filter out field data sets suspected of containing calibration errors [Carder, 1999]. They found that spectral ratios of $R_{rs}(\lambda)$ for clear, subtropical or tropical waters lie above the line $r(412,443) = 0.95 * r(443,551)^{0.16}$ for $r(443,551) > 3.0$, where $r(412,443) = R_{rs}(412)/R_{rs}(443)$ and $r(443,551) = R_{rs}(443)/R_{rs}(551)$. $R_{rs}(\lambda)$, the remote-sensing reflectance at wavelength λ , is defined as $L_w(\lambda)/E_d(\lambda)$, where $L_w(\lambda)$ is the water-leaving radiance and $E_d(\lambda)$ is the downwelling irradiance just above the sea surface. Ocean regions that are reasonably well understood can be studied once the potential problems of instrument calibration and atmospheric correction have been eliminated. For the warm-water central gyres the data should conform to the CZCS algorithm [Gordon, 1983] for chlorophyll-like pigments:

$$Chl_a = 1.13 * [R_{rs}(443) / R_{rs}(551)]^{-1.71}$$

Here the wavelengths represent those on MODIS, while CZCS and SeaWiFS use 550 and 555 nm, respectively, instead of 551 nm for the denominator. All forms are statistically equivalent as the effects of small wavelength changes are insignificant relative to the variance of data about this empirical curve, and MODIS uses a bandwidth that is half the 20 nm width of the other two sensors.

Using SeaWiFS and AVHRR global data can be used as inputs to the MODIS atmospheric correction and ocean color algorithms [Hawes et al., 1990]. As a first step we use the Level 2 normalized water-leaving radiance, chlorophyll a , and gelbstoff absorption coefficient products to evaluate the performance of SeaWiFS and the performance of various algorithms. Data from two central gyre locations and the Mediterranean Sea, as well as the global data, are used in this process. Retrievals from three other chlorophyll a algorithms are compared: the SeaWiFS OC2 [O'Reilly, 1998]; the MODIS Case 1 chlorophyll algorithm, called chlor_MODIS (D. Clark, ATBD-MOD-19, Bio-optical algorithms Case 1 waters); and the MODIS Case 2 chlorophyll algorithm, called chlor_a_3 [Carder, 1999]. Like Equation 1, OC2 uses two wavelengths, but they are 488 and 551 nm, and second- and third-order terms are

included. chlor_MODIS uses four wavelengths, 443, 488, 531, and 551 nm, and a third-order regression. chlor_a_3 uses 412, 443, 488, and 551 nm, separating the chlorophyll *a* concentration from effects due to absorption by gelbstoff, or colored dissolved organic matter (CDOM).

Figure 1 shows histograms of the chlorophyll distributions from 0 to 1.0 mg m⁻³ for three algorithms: chlor_a_3, chlor_MODIS, and OC2. Mode values are 0.075, 0.105, and 0.095 mg m⁻³ for chlor_a_3, chlor_MODIS, and OC2, respectively. The chlor_a_3 mode is close to what we expect to find in much of the world's oceans, i.e., in the central gyres (see Table 1 and section 3.2 below). chlor_a_3 has a pronounced bimodal distribution, with the secondary mode at 0.305 mg m⁻³. This is near the mode value of around 0.25 mg m⁻³ found for an *in situ* data set of pigment concentrations from the Southern Ocean⁶. The other two algorithms show less pronounced secondary modes.

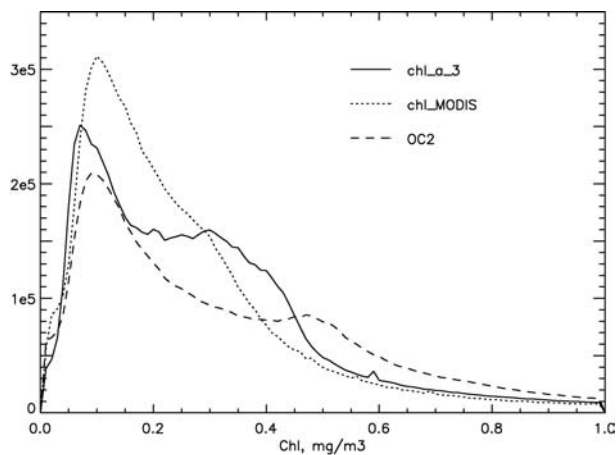


Figure 1. Global chlorophyll frequency distributions for three algorithms for the data collected on 2 and 3 July 1998. (after Hawes et al., 2000)

3.3.2 Mediterranean Sea. The southeast, central Mediterranean Sea behaves in the summer time in an optical manner similar to the oligotrophic waters of the central gyres, having low chlorophyll and relatively low gelbstoff values. The location at times suffers from influxes of Saharan dust. We used satellite data from sequential days (Box 1 vs. Box 2 in Fig. 2) to observe the effects that blue-absorbing Saharan aerosols have on retrievals of the absorption coefficient due to Colored dissolved organic matter (CDOM) or gelbstoff at 400 nm, $a_g(400)$, and spectral ratios of R_{rs} . Figure 2 is a composite of $a_g(400)$

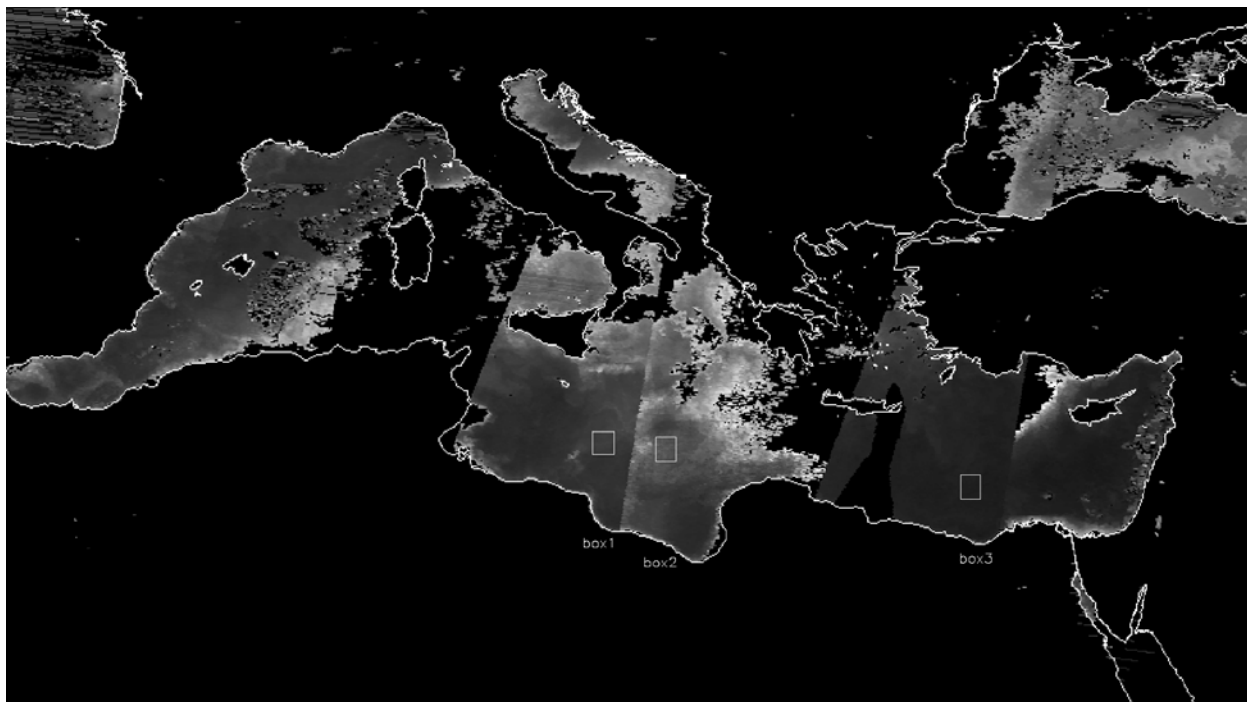


Figure 2. Gelbstoff retrieval sites over Mediterranean Sea. (after Hawes et al. 2000)

retrievals for 2 and 3 July 1998, with sharp, linear gradients occurring at satellite swath edges when the retrievals on consecutive days are inconsistent (satellite over-passes for adjacent swaths occur on alternating days with SeaWiFS). Thus the regions depicted by Box 1 and Box 2 in Figure 2 were measured on different days. The mean aerosol optical thickness values, $\tau_a(865)$, are 0.261 for Box 1 and 0.357 for Box 2, indicating different aerosol concentrations for the consecutive days.

Blue-absorbing aerosols will have a large effect on scenes derived with atmospheric-correction codes that do not take aerosol absorption into account (i.e., SeaWiFS and MODIS atmospheric correction algorithms) by lowering the at-sensor radiance in the blue end of the spectrum. A result of this inaccuracy is to increase the value of $a_g(400)$ predicted by the algorithm, since gelbstoff also absorbs strongly in the blue. This effect is apparent in the sharp linear gradients in the gelbstoff-absorption image (Fig. 2). Thus, *the aerosol absorption problem can also be analyzed by the effects on spectral ratios of R_{rs}* (Fig. 3). Note that ratios from Box 1 are less affected than those from the nearby Box 2, which cascade toward $r(412,443)$ values of 0.1 or less. Note also that the relatively unaffected data from Box 3 approximate the data positions on the corresponding chart for the Bermuda Atlantic Time-Series (BATS) ratios. Since non-absorbing aerosols would perturb the numerator and denominator values of $r(412,443)$ more or less equally, and would not lead to the catastrophic cascading behavior seen in the R_{rs} ratios for Box 2 of Figure 3, we conclude that these effects are diagnostic of blue-absorbing aerosols similar to Saharan dust.

A note of caution regarding use of SeaWiFS data processed before 2002 must be made, however. New calibration tables for SeaWiFS indicate pre_2002 data for the 412 nm channel are as much as 1.7% too low. Since molecular path radiance in the atmosphere can represent 80% to 90% of L_t , the resulting underestimation in $L_w(412)$ can range from 9.5% to 17%, moving the data points in Figure 3 closer to the dashed line. Data from the Hawaii Ocean Time Series (Hawes et al., 2000) fell directly on the line. A 17% increase would place those data above the line as expected (Carder et al. 1999) for summer Case 1 data sets in the subtropics .

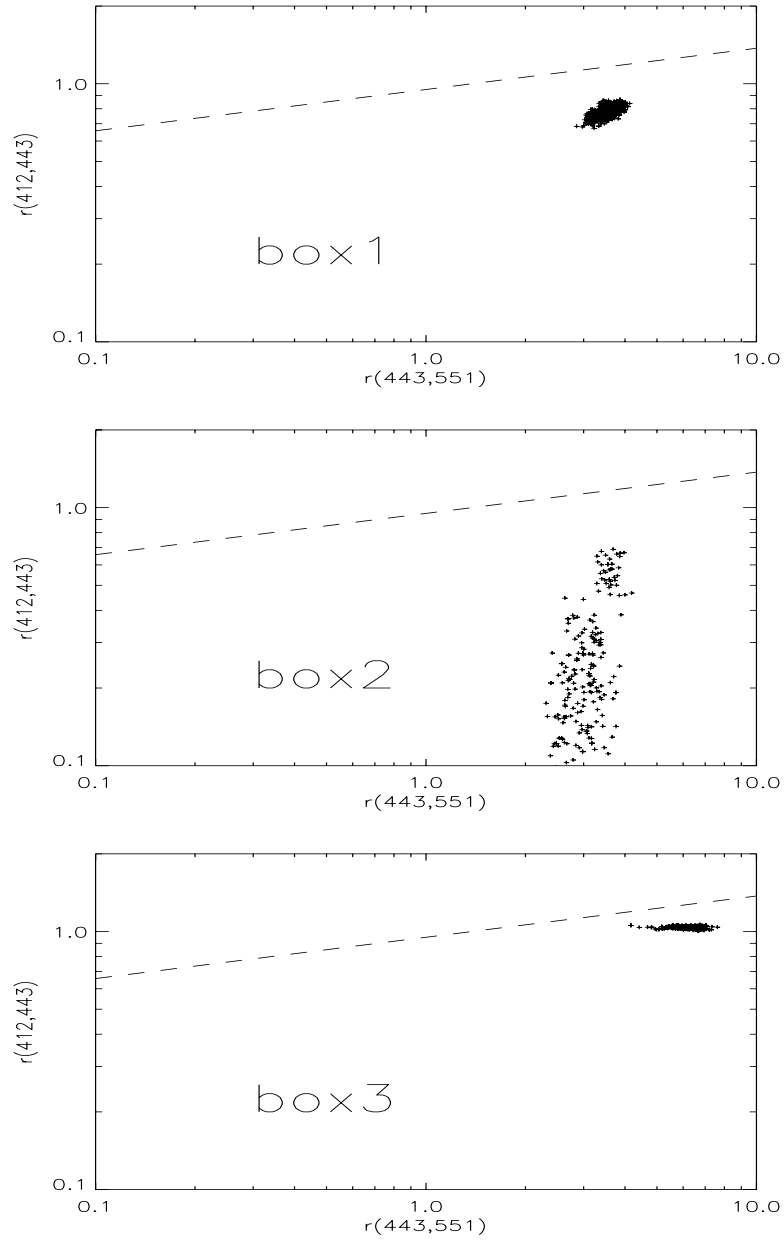


Figure 3 $r(412,443)$ vs. $r(443,551)$ for the 25x25 pixel regions indicated in Figure 2. (after Hawes et al., 2000)

3.4 Mathematical Description of the Algorithm

The clear-water epsilon flag will therefore be a combination of two algorithms. The first will be a simple test of the clear-water aerosol epsilon. If this variable falls below a threshold value, the data will be flagged for examination by the second algorithm. This threshold value is currently set at 1.00 but is expected to increase after reviewing MODIS retrievals over dusty regions. Thus, the aerosol epsilon expected of airborne African mineral dust at any spaceborne sensor (i.e., MODIS, MERIS, SeaWiFS, OCTS) wavelength will be computed,

$$\varepsilon(531,667) \equiv \frac{\rho_{as}(531)}{\rho_{as}(667)} = \frac{\omega_a(531) \cdot \tau_a(531) \cdot P(\Theta,531)}{\omega_a(667) \cdot \tau_a(667) \cdot P(\Theta,667)},$$

Data which have been “flagged” by the first algorithm will then be tested by the ratio $r(412;443)$ vs $r(433, 551)$, considered a diagnostic of blue-absorbing aerosols over waters with $r(443,551) > 2.5$. We need to better understand the behaviour of this ratio with the presence of different types of mineral dust but it is quite clear that the catastrophic behaviour of $r(412;443)$ in Figure 3 is due to the presence of blue-absorbing mineral dust. We believe that the ratio itself contains enough information to deduce the aerosol single-scattering albedo and, from this, perhaps the iron content in the aerosol. Success of this latter point will achieve both goals of the clear-water epsilon algorithm. The comprehensive spatial and temporal coverage by SeaWiFS and MODIS would lead to global maps of iron delivery to the ocean.

3.4.1 Numerical computational considerations

We modified the normalized water-leaving radiances, $L_{wn}(\lambda_i)$, at 520, 550, and 670 nm (which are designated *a priori* for the CZCS) to 531, 551, and 667 nm for MODIS by

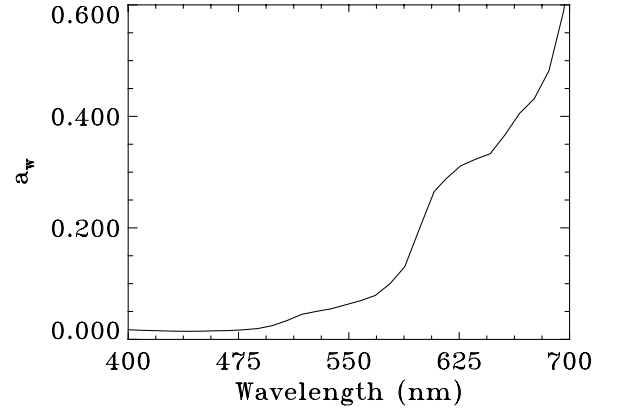
$$L_{wn}(531) = \frac{a_w(520)}{a_w(531)} L_{wn}(520)$$

$$L_{wn}(551) = L_{wn}(550) \quad ,$$

$$L_{wn}(667) = \frac{a_w(670)}{a_w(667)} L_{wn}(670)$$

where $a_w(\lambda)$ are water absorption coefficients

from Smith and Baker (1981).



3.4.2 Calibration and validation

Ground-based radiometric measurements of sky radiance and atmospheric transmittance contain sufficient information to derive the complete set of aerosol radiative parameters: optical thickness $\tau(\lambda)$; single-scattering albedo $\omega_0(\lambda)$, the ratio of scattering to extinction (absorption + scattering); and phase function $P(\Theta, \lambda)$, the angular distribution of scattered light [Dubovik and King, 2000; Wang and Gordon, 1993], where λ represents wavelength. AERONET will serve a valuable diagnostic tool of our algorithm as it operates over 150 sites over the globe. Several sites (Bermuda, Barbados, Cape Verde, Bahrain, Solar Village and Ft. Jefferson, Dry Tortugas) consistently experience the passage of mineral dust. A climatology of dust radiative characteristics can therefore be obtained to test the robustness of our clear-water epsilon algorithm in dealing with different blue-absorbing aerosol types, and afford validation of both aerosol optical depth and epsilon values.

3.4.3 Variance or uncertainty estimates

Uncertainties of less than 0.05 for $\epsilon(531,667)$ within the range 0.9 to 1.5 are estimated at present for clear-water regions. A comparison of $\epsilon(531,667)$ with $\epsilon(750,865)$ is necessary to ascertain the sensitivity of epsilon at shorter wavelengths to the presence of dust, compared to that of 750 nm. Its sensitivity to aerosol optical depths also needs to be quantified.

3.4.5 Output product

The output product in its simplest form will be maps of clear-water epsilons, with low values indicative of desert aerosols or very large marine aerosols. High values with large $\tau_a(865)$ values are indicative of regions of biomass burning (e. g. see Holben et al. 2001). These values provide a flag for potential problems with L_w values calculated using Angström exponent-based extrapolations from the infra-red for aerosol radiance values into the visible. Recent work [Catrall, 2002; Dubovik et al., 2002; Holben et al., 1998; Kaufman et al., 2001; Tanré et al., 2001] suggest that the single-scattering albedo of African dust is about 0.97 at 531 nm. At this wavelength range (531;667), it is unlikely that absorption will perturb the clear-water epsilon enough to distinguish directly dust absorption effects. However, epsilons near unity will be strong candidates for review by either the $r(412;443)$ versus $r(443;551)$ approach or examining "pre-dust" chlorophyll fields later perturbed by the presence of blue-absorbing desert aerosols. These approaches can be corroborated by AERONET radiometer sites, where air mass identification is possible from measurements of the aerosol optical depth and sky radiance [Dubovik et al., 2002; Reddy et al., 1990; Smirnov et al., 1998; Tanré et al., 1988; von Hoyningen-Huene and Raabe, 1987].

We are extending the use of the "clear water" radiance approach to regions with chlorophyll concentrations as high as $0.5\text{-}1 \text{ mg m}^{-3}$ (see Appendix A). This will increase the useful range of applicability of the algorithm with only a modest increase in the expected error (8% to 13%) in $L_{wn}(531)$. For major dust outbreaks where the major flux of iron to the ocean might be expected, increases in $L_a(531)$ will be far greater than the increase in uncertainty in $L_{wn}(531)$.

4.0 Constraints, Limitations and Assumptions

Gordon and Castaño (1987) have shown that errors associated with the quasi-single scattering model result from multiple scattering effects on $L_a(\lambda)$ and the assumed independence of $L_r(\lambda)$ and $L_a(\lambda)$. Therefore, when both the solar zenith angle and the Angström exponent are increased, care must be taken in interpreting the data, or else a multiple scattering model should be used.

When pigment concentrations are larger than 1 mg m^{-3} (to be extended to 2, see Appendix A), L_{wn} is no longer known for 531 and 551 nm so this method cannot be applied. Thus, the algorithm will be effective only over clear (open ocean) water.

This algorithm will only be effective for dust that absorbs in a known and predictable manner over the wavelength range involved. Transport and settling mechanisms must be carefully considered in atmospheric correction of satellite imagery over oligotrophic waters. Thus, an extensive database of optical signatures is being pursued using AERONET data.

The physics of the problem will be slightly different for a nadir-viewing sensor. The Rayleigh scattering term will be proportionately larger as it is not attenuated as much by the aerosol layer. Dust absorption effects will comparatively be perhaps only 10-20% of that observed in ground-based measurements. Concomitantly, aerosol dust storms often extend to 6 km [Reinersman and Carder, 1995], confounding the simplifying assumption of clearly-defined atmospheric layers. Monte Carlo simulations [Reinersman and Carder, 1995] will be pursued in the future to examine such possible effects.

5.0 Products

These investigations are expected to produce several primary results:

1. An optical characterization of a Saharan dust aerosol that has undergone long and medium range transport.
2. An improved determination of chlorophyll pigment concentration in images where such dust is present
3. Detailed histories of absorption and scattering in the presence of dust, as functions of scan and view angles, aerosol optical depths, aerosol model.
4. A possible estimation of iron flux to the ocean.

The derived optical characteristics and characteristic epsilon values will afford their use in MODIS and SeaWiFS image correction, with sources based upon climatology and region. Saharan dust closer to source regions and Gobi dust can be characterized once this method has proven successful for long-range Saharan dust. The unimodal size distribution expected for long-range Saharan dust will simplify this particular investigation (Cattrall 2002).

5.0 Research Timetable

Our retrievals of mineral dust single-scattering albedo and phase function from the Florida Keys will be used to simulate satellite sensor radiance. Further results from a global sky/sun photometer network [Holben *et al.*, 1998] will also be useful for epsilon evaluation at sites that experience frequent passage of African dust. In order to investigate a large range of solar zenith angles, aerosol types and optical depths, other clear-water island areas will be

included once the algorithm has performed satisfactorily. This will also aid in investigating the change in optical signature from the same dust source, such as the Gobi or Saharan Desert.

References

- Acharya, P.K., A. Berk, L.S. Bernstein, J.W. Matthew, S.M. Adler-Golden, D.C. Robertson, G.P. Anderson, J.H. Chetwynd, F.X. Kneizys, E.P. Shettle, L.W. Abreu, W.O. Gallery, J.E.A. Selby, and S.A. Clough, MODTRAN User's Manual Versions 3.7 and 4.0, Space Vehicles Directorate, Air Force Materiel Command, Hanscom AFB, MA, 1998.
- Ångström, A., The parameters of atmospheric turbidity, *Tellus*, *16* (1), 64-75, 1964.
- Archer, D.E., and K. Johnson, A model of the iron cycle in the ocean, *Global Biogeochemical Cycles*, *14* (1), 269-279, 2000.
- Arimoto, R., R.A. Duce, B.J. Ray, W.G. Ellis Jr., J.D. Cullen, and J.T. Merrill, Trace elements in the atmosphere over the North Atlantic, *Journal of Geophysical Research*, *100* (D1), 1199-1213, 1995.
- Betzer, P.R., K.L. Carder, R.A. Duce, J.T. Merrill, N.W. Tindale, M. Uematsu, D.K. Costello, R.W. Young, R.A. Feely, and et-al, Long-range transport of giant mineral aerosol particles, *Nature*, *336* (6199), 568-571, 1988.
- Biggar, S.F., K.J. Thome, P.N. Slater, L.K. Balick, and C.J. Golanics, Solar-radiation-based absolute calibration of optical sensors: SeaWIFS and a Daedalus 1268, in *IGARSS-94*, pp. 1992-1994, Pasadena, California, 1994.
- Boyd, P.W., A.J. Watson, C.S. Law, E.R. Abraham, T. Trull, R. Murdoch, D.C.E. Bakker, A.R. Bowie, K.O. Buesseler, H. Chang, M. Charette, P. Croot, and K.D.e. al., A mesoscale phytoplankton bloom in the polar Southern Ocean stimulated by iron fertilization, *Nature*, *407*, 695-702, 2000.

- Carder, K.L., W.W. Gregg, D.K. Costello, K. Haddad, and J.M. Prospero, Determination of Saharan dust radiance and chlorophyll from CZCS imagery, *Journal of Geophysical Research*, 96 (D3), 5369-5378, 1991.
- Carlson, R.N., and S.G. Benjamin, Radiative heating rates for Saharan dust, *Journal of Geophysical Research*, 37, 193-213, 1980.
- Carlson, T.N., and R.S. Caverly, Radiative characteristics of Saharan dust at solar wavelengths, *Journal of Geophysical Research*, 82, 3141-3152, 1977.
- Carlson, T.N., and J.M. Prospero, The large-scale movement of Saharan air outbreaks over the northern equatorial Pacific, *Journal of Applied Meteorology*, 11, 283-297, 1972.
- Cattrall, C., Retrieval of columnar aerosol single-scattering albedo and phase function from sky radiance over the ocean: Measurements of African dust, Ph.D. thesis, University of South Florida, St. Petersburg, 2002.
- Charlson, R.J., S.E. Schwartz, J.M. Hales, R.D. Cess, J.A. Coakley Jr., J.E. Hansen, and D.J. Hofmann, Climate forcing by anthropogenic aerosols, *Science*, 255, 423-430, 1992.
- Chiapello, I., J.M. Prospero, J.R. Herman, and N.C. Hsu, Detection of mineral dust over the North Atlantic Ocean and Africa with the Nimbus 7 TOMS, *Journal of Geophysical Research*, 104 (D8), 9277-9291, 1999.
- Claquin, T., M. Schulz, and Y.J. Balkanski, Modeling the mineralogy of atmospheric dust sources, *Journal of Geophysical Research*, 104 (D18), 22,243-22,256, 1999.
- Coale, K.H., K.S. Johnson, S.E. Fitzwater, R.M. Gordon, S. Tanner, F.P. Chavez, L. Ferioli, C. Sakamoto, P. Rogers, F.J. Millero, P. Steinberg, P. Nightingale, D.

- Cooper, W.P. Cochlan, M.R. Landry, J. Constantinou, G. Rollwagen, A. Trasvina, and R. Kudela, A massive phytoplankton bloom induced by an ecosystem-scale iron fertilization experiment in the equatorial Pacific Ocean, *Nature*, 383, 495-501, 1996.
- d'Almeida, G.A., On the variability of desert aerosol radiative characteristics, *Journal of Geophysical Research*, 92 (D3), 3017-3026, 1987.
- Devaux, C., A. Vermeulen, J.L. Deuzé, P. Dubuisson, M. Herman, R. Santer, and M. Verbrugghe, Retrieval of aerosol single-scattering albedo from ground-based measurements: Application to observational data, *Journal of Geophysical Research*, 103 (D8), 8753-8761, 1998.
- Dubovik, O., B.N. Holben, T.F. Eck, A. Smirnov, Y.J. Kaufman, M.D. King, D. Tanré, and I. Slutsker, Variability of absorption and optical properties of key aerosol types observed in worldwide locations, *J. Atmos. Sci*, 59, 590-608, 2002.
- Dubovik, O., and M.D. King, A flexible inversion algorithm for retrieval of aerosol optical properties from Sun and sky radiance measurements, *Journal of Geophysical Research*, 105 (D16), 20,673-20,696, 2000.
- Dubovik, O., A. Smirnov, B.N. Holben, M.D. King, Y.J. Kaufman, T.F. Eck, and I. Slutsker, Accuracy assessments of aerosol optical properties retrieved from Aerosol Robotic Network (AERONET) Sun and sky radiance measurements, *Journal of Geophysical Research*, 105 (D8), 9791-9806, 2000.
- Duce, R.A., and N.W. Tindale, Atmospheric transport of iron and its deposition in the ocean, *Limnology and Oceanography*, 36, 1715-1726, 1991.

- Eck, T.F., B.N. Holben, J.S. Reid, O. Dubovik, A. Smirnov, N.T. O'Neill, I. Slutsker, and S. Kinme, Wavelength dependence of the optical depth of biomass burning, urban, and desert dust aerosols, *Journal of Geophysical Research*, 104, 31,333-31,350, 1999.
- Ehsani, A.R., Design of a microprocessor based sun-tracking multi-channel solar radiometer system, M.Sc. thesis, University of Arizona, Tucson, AZ, 1992.
- Fouquart, Y., B. Bonnel, J.C. Brogniez, L. buriez, L. Smith, and J.J. Morcrette, Observations of Saharan aerosols: Results of ECLATS field experiment. Part II: Broadband radiative characteristics of the aerosols and vertical radiative flux divergence, *J. Clim. Appl. Met.*, 25, 28-37, 1986.
- Fukushima, H., and M. Toratami, Asian dust aerosol: Optical effect on satellite ocean color signal and a scheme of its correction, *Journal of Geophysical Research*, 102 (D14), 17,119-17,130, 1997.
- Fung, I.Y., S.K. Meyn, I. Tegen, S.C. Doney, J.G. John, and J.K.B. Bishop, Iron supply and demand in the upper ocean, *Global Biogeochemical Cycles*, 14 (1), 281-295, 2000.
- Gao, Y., Y.J. Kaufman, D. Tanré, D. Kolber, and P.G. Falkowski, Seasonal distributions of aeolian iron fluxes to the global ocean, *Geophysical Research Letters*, 28 (1), 29-32, 2001.
- Gillespie, J.B., and J.D. Lindberg, Ultraviolet and visible imaginary refractive index of strongly absorbing atmospheric particulate matter, *Applied Optics*, 31 (12), 2112-2115, 1992.

- Glaccum, R.A., and J.M. Prospero, Saharan aerosols over the torpical north Atlantic - Mineralogy, *Marine Geology*, 37, 295-321, 1980.
- Gordon, H.R., MODIS Normalized Water-leaving Radiance Algorithm Theoretical Basis Document, University of Miami, 1994.
- Gordon, H.R., Atmospheric correction of ocean color imagery in the Earth Observing System era, *Journal of Geophysical Research*, 102 (D14), 17,081-17,106, 1997.
- Gordon, H.R., O.B. Brown, R.H. Evans, J.W. Brown, R.C. Smith, K.S. Baker, and D.K. Clark, A semianalytic radiance model of ocean color, *Journal of Geophysical Research*, 93 (C9), 10,909-10,924, 1988.
- Gordon, H.R., R.M. Chomko, and C. Moulin, Advanced atmospheric correction algorithms, in *Ocean Optics XV*, Monaco, 2000.
- Gordon, H.R., and D.K. Clark, Clear water radiances for atmospheric correction of coastal zone color scanner imagery, *Applied Optics*, 20 (24), 4175-4179, 1981.
- Gordon, H.R., D.K. Clark, J.W. Brown, O.B. Brown, R.H. Evans, and W.W. Broenkow, Phytoplankton pigment concentrations in the Middle Atlantic Bight: comparison of ship determinations and CZCS estimates, *Applied Optics*, 22 (1), 20-36, 1983.
- Gordon, H.R., and M. Wang, Surface-roughness considerations for atmospheric correction of ocean color sensors. I: The Rayleigh-scattering component, *Applied Optics*, 31 (21), 4247-4260, 1992a.
- Gordon, H.R., and M. Wang, Surface-roughness considerations for atmospheric correction of ocean color sensors. II: Error in the retrieved water-leaving radiance, *Applied Optics*, 31 (21), 4261-4267, 1992b.

- Gordon, H.R., and M. Wang, Influence of oceanic whitecaps on atmospheric correction of ocean-color sensors, *Applied Optics*, 33 (33), 7754-7763, 1994a.
- Gordon, H.R., and M. Wang, Retrieval of water-leaving radiance and aerosol optical thickness over the oceans with SeaWiFS: A preliminary algorithm, *Applied Optics*, 33, 443-452, 1994b.
- Gordon, H.R., and T. Zhang, How well can radiance reflected from the ocean-atmosphere system be predicted from measurements at the sea surface?, *Applied Optics*, 35 (33), 6527-6543, 1996.
- Gregg, W.W., and K.L. Carder, A simple spectral solar irradiance model for cloudless maritime atmospheres, *Limnology and Oceanography*, 35 (8), 1657-1675, 1990.
- Hansen, A.D.A., V.N. Kapustin, V.M. Kopeikin, D.A. Gillette, and B.A. Bodhaine, Optical absorption by aerosol black carbon and dust in a desert region of Soviet Central Asia, *Atmospheric Environment*, 27A, 2527-2531, 1993.
- Hansen, J., W. Rossow, B. Carlson, A. Lacis, L. Travis, A. Del Genio, I. Fung, B. Cairns, M. Mischenko, and M. Sato, Low-cost long-term monitoring of global climate change forcings and feedbacks, *Climatic Change*, 31, 247-271, 1995.
- Hansen, J., M. Sato, and R. Ruedy, Radiative forcing and climate response, *Journal of Geophysical Research*, 102 (D6), 6831-6864, 1997.
- Hansen, J., M. Sato, R. Ruedy, A. Lacis, and V. Oinas, Global warming in the twenty-first century: An alternative scenario, *Proceedings of the National Academy of Sciences*, 97 (18), 9875-9880, 2000.

- Hawes, S.K., K.L. Carder, R.H. Evans, “MODIS CDOM and chlorophyll: a first look using SeaWiFS and AVHRR data”, in *Earth Observing Systems V*, W.L. Barnes, Editor, Proc. SPIE 4135, 403-410 (2000).
- Haywood, J., and O. Boucher, Estimates of the direct and indirect radiative forcing due to tropospheric aerosols: A review, *Reviews of Geophysics*, 38 (4), 513-543, 2001.
- Henry, J.A., K.M. Portier, and J. Coyne, *The Climate and Weather of Florida*, 279 pp., Pineapple Press, Inc., Sarasota, Florida, 1994.
- Herman, J., P.K. Bhartia, O. Torres, C. Hsu, C. Seftor, and E. Celarier, Global distribution of UV-absorbing aerosols from Nimbus-7/TOMS data, *Journal of Geophysical Research*, 102 (D14), 16,911-16,922, 1997.
- Holben, B.N., T.F. Eck, I. Slutsker, D. Tanré, J.P. Buis, A. Setzer, E. Vermote, J.A. Reagan, Y.J. Kaufman, T. Nakajima, F. Lavenu, I. Jankowiak, and A. Smirnov, AERONET - a federated instrument network and data archive for aerosol characterization, *Remote Sensing of the Environment*, 66, 1-16, 1998.
- Holben, B.N., D. Tanré, A. Smirnov, T.F. Eck, I. Slutsker, N. Abuhassan, W.W. Newcomb, J.S. Schafer, B. Chatenet, F. Lavenu, Y.J. Kaufman, J.V.d. Castle, A. Setzer, B. Markham, D. Clark, R. Frouin, R. Halthore, A. Karnieli, N.T. O'Neill, C. Pietras, R.T. pinker, K. Voss, and G. Zibordi, An emerging ground-based aerosol climatology: Aerosol optical depth from AERONET, *Journal of Geophysical Research*, 106 (D11), 12,067-12,097, 2001.
- Hoppel, W.A., J.W. Fitzgerald, G.M. Frick, R.E. Larson, and E.J. Mack, Aerosol size distributions and optical properties found in the marine boundary layer over the Tatlantic Ocean., *Journal of Geophysical Research*, 95 (D4), 3659-3686, 1990.

- Husar, R.B., J.M. Prospero, and L.L. Stowe, Characterization of tropospheric aerosols over the oceans with the NOAA advanced very high resolution radiometer optical thickness operational product, *Journal of Geophysical Research*, 102 (D14), 16,889-16,909, 1997.
- Junge, C., *Air Chemistry and Radioactivity*, Academic Press, 1963.
- Kahn, R., P. Banerjee, D. McDonald, and D.J. Diner, Sensitivity of multiangle imaging to aerosol optical depth and to pure-particle size distribution and composition over ocean, *Journal of Geophysical Research*, 103 (D14), 32,195-32,213, 1998.
- Karyampudi, V.M., and T.N. Carlson, Analysis and numerical simulation of the Saharan Air Layer and its effect on easterly wave disturbances, *Journal of the Atmospheric Sciences*, 45 (21), 3102-3136, 1988.
- Kaufman, Y.J., D. Tanré, O. Dubovik, A. Karnieli, and L.A. Remer, Absorption of sunlight by dust as inferred from satellite and ground-based remote sensing, *Geophysical Research Letters*, 28 (8), 1479-1482, 2001.
- Kaufman, Y.J., D. Tanré, H.R. Gordon, T. Nakajima, J. Lenoble, R. Frouin, H. Grassl, B.M. Herman, M.D. King, and P.M. Teillet, Passive remote sensing of tropospheric aerosol and atmospheric correction for the aerosol effect, *Journal of Geophysical Research*, 102 (D14), 16,815-16,830, 1997.
- Korotaev, G.K., S.M. Sakerin, A.M. Ignatov, L.L. Stowe, and E.P. McClain, Sunphotometer observations of aerosol optical thickness over the North Atlantic from a Soviet research vessel for validation of satellite measurements, *Jour. Atmos. Oceanic Technol.*, 10 (725-735), 1993.

- Levin, Z., J.H. Joseph, and Y.Mekler, Properties of Sharav (Khamsim) dust - comparison of optical and direct sampling data, *Journal of the Atmospheric Sciences*, 37, 882-891, 1980.
- Mahowald, N., K. Kohfeld, M. Hansson, Y. Balkanski, S.P. Harrison, I.C. Prentice, M. Schulz, and H. Rodhe, Dust sources and deposition during the last glacial maximum and current climate: A comparison of model results with paleodata from ice cores and marine sediments, *Journal of Geophysical Research*, 104 (D123), 15,895-15,916, 1999.
- Martin, J.H., Glacial-interglacial CO₂ change: The iron hypothesis, *Paleoceanography*, 5 (1), 1-13, 1990.
- Martin, J.H., and R.M. Gordon, Northeast Pacific iron distributions in relation to phytoplankton productivity, *Deep Sea Research*, 35 (A), 177-196, 1988.
- Martin, J.H., R.M. Gordon, and S.E. Fitzwater, The case for iron, *Limnology and Oceanography*, 36, 1793-1802, 1991.
- Miller, R.L., and I. Tegen, Climate response to soil dust aerosols, *Journal of Climate*, 11, 3247-3267, 1998.
- Mishchenko, M.I., I.V. Geogdzhayev, B. Cairns, W.B. Rossow, and A.A. Lacis, Aerosol retrievals over the ocean by use of channels 1 and 2 AVHRR data: Sensitivity analysis and preliminary results, *Applied Optics*, 38 (36), 7325-7341, 1999.
- Mishchenko, M.I., L.D. Travis, R.A. Kahn, and R.A. West, Modeling phase functions for dustlike tropospheric aerosols using a shape mixture of randomly oriented

- polydisperse spheroids, *Journal of Geophysical Research*, 102 (D14), 16,831-16,848, 1997.
- Moulin, C., H.R. Gordon, V.F. Banzon, and R.H. Evans, Assessment of Saharan dust absorption in the visible from SeaWiFS imagery, *Journal of Geophysical Research*, 106 (D14), 18,239-18,250, 2001a.
- Moulin, C., H.R. Gordon, R.M. Chomko, V.F. Banzon, and R.H. Evans, Atmospheric correction of ocean color imagery through thick layers of Saharan dust, *Geophysical Research Letters*, 28 (1), 5-8, 2001b.
- Myhre, G., and F. Stordal, Global sensitivity experiments of the radiative forcing due to mineral aerosols, *Journal of Geophysical Research*, 106 (D16), 18,193-18,204, 2001.
- Ogren, J.A., A systematic approach to *in situ* observations of aerosol properties, in *Aerosol Forcing of Climate*, edited by R.J. Charlson, and J. Heintzenberg, pp. 215-226, John Wiley, New York, 1995.
- Ott, S.-T., A. Ott, D.W. Martin, and J.A. Young, Analysis of a trans-Atlantic Saharan dust outbreak based on satellite and GATE data, *Monthly Weather Review*, 119, 1832-1850, 1991.
- Patterson, E.M., Complex index of refraction between 300 and 700 nm for Saharan aerosols, *Journal of Geophysical Research*, 82 (21), 3153-3160, 1977.
- Patterson, E.M., Optical properties of the crustal aerosol: relation to chemical and physical characteristics, *Journal of Geophysical Research*, 82 (15), 2074-2082, 1981.

- Perlwitz, J., I. Tegen, and R.L. Miller, Interactive soil dust aerosol model in the GISS GCM 1. Sensitivity of the soil dust cycle to radiative properties of soil dust aerosols, *Journal of Geophysical Research*, 106 (D16), 18,167-18,192, 2001.
- Petit, J.-R., J. Jouzel, D. Raynaud, N.I. Barkov, J.M. Barnola, I. Basile, M. Bender, J. Chapellaz, M. Davis, G. Delaygue, M. Delmotte, V.M. Kotlyakov, M. Legrand, V.Y. Lipenkov, C. Lorius, L. Pepin, C. Ritz, E. Saltzman, and M. Stievenard, Climate and atmospheric history of the past 420,000 years from the Vostok ice core, Antarctica, *Nature*, 399 (6735), 429-436, 1999.
- Prospero, J.M., Arid regions as sources of mineral aerosols in the marine atmosphere, in *Desert Dust: Origin, Characteristics, and Effect on Man*, edited by T.L. Péwé, pp. 303, Geological Society of America, Boulder, CO, 1981.
- Prospero, J.M., Long-term measurements of the transport of African mineral dust to the southeastern United States: Implications for regional air quality, *Journal of Geophysical Research*, 104 (D13), 15,917-15,927, 1999.
- Prospero, J.M., I. Olmez, and M. Ames, Al and Fe in PM 2.5 and PM 10 suspended particles in south-central Florida: The impact of the long range transport of African mineral dust, *Water, Air and Soil Pollution*, 125 (1-4), 291-317, 2001.
- Reddy, P.J., F.W. Kreiner, J.J. DeLuisis, and Y. Kim, Aerosol optical depths over the Atlantic derived from shipboard sunphotometer observations during the 1988 Global Change Expedition, *Global Biogeochemical Cycles*, 4 (3), 225-240, 1990.
- Reinersman, P.N., and K.L. Carder, Monte Carlo simulation of the atmospheric point spread function with application to correction for adjacency effect, *Applied Optics*, 34 (21), 4453-4471, 1995.

- Savoie, D.L., and J.M. Prospero, Aerosol concentration statistics for the Northern Tropical Atlantic, *Journal of Geophysical Research*, 82 (37), 5954-5964, 1977.
- Schütz, L., Long-range transport of desert dust with special emphasis on the Sahara, in *Ann. N.Y. Acad. Sci.*, edited by T.N. Kneip, and P.J. Liou, pp. 515-532, New York, 1980.
- Schütz, L., R. Jaenicke, and H. Pietrek, Saharan dust transport over the North Atlantic Ocean, in *Desert Dust: Origin, Characteristics, and Effects on Man*, edited by T.L. Péwé, Geological Society of America, Boulder, CO, 1981.
- Shettle, E.P., and R.W. Fenn, Models for the aerosols of the lower atmosphere and the effects of humidity variations on their optical properties, Air Force Geophysics Laboratory, 1979.
- Smirnov, A., B.N. Holben, I. Slutsker, E.J. Welton, and P. Formenti, Optical properties of Saharan dust during ACE 2, *Journal of Geophysical Research*, 103 (D21), 28,079-28,092, 1998.
- Sokolik, I.N., and O.B. Toon, Direct radiative forcing by anthropogenic airborne mineral aerosols, *Nature*, 381 (681-683), 1996.
- Sokolik, I.N., and O.B. Toon, Incorporation of mineralogical composition into models of the radiative properties of mineral aerosol from UV to IR wavelengths, *Journal of Geophysical Research*, 104 (D8), 9423-9444, 1999.
- Sokolik, I.N., D.M. Winker, G. Bergametti, D.A. Gillette, G. Carmichael, Y.J. Kaufman, L. Gomes, L. Schuetz, and J.E. Penner, Introduction to special section: Outstanding problems in quantifying the radiative impacts of mineral dust, *Journal of Geophysical Research*, 106 (D16), 18,015-18,027, 2001.

- Stowe, L.L., A.M. Ignatov, and R.R. Singh, Development, validation, and potential enhancements to the second-generation operational aerosol product at the National Environmental Satellite, Data, and Information Service of the National Oceanic and Atmospheric Administration, *Journal of Geophysical Research*, 102 (D14), 16,923-16,934, 1997.
- Tanré, D., C. Devaux, M. Herman, R. Santer, and J.Y. Gac, Radiative properties of desert aerosols by optical ground-based measurements at solar wavelengths, *Journal of Geophysical Research*, 93 (D11), 14,223-14,231, 1988.
- Tanré, D., M. Herman, and Y.J. Kaufman, Information on aerosol size distribution contained in solar reflected spectral radiances, *Journal of Geophysical Research*, 101 (D14), 19,043-19,060, 1996.
- Tanré, D., Y.J. Kaufman, B.N. Holben, B. Chatenet, A. Karnieli, F. Lavenu, L. Blarel, O. Dubovik, L.A. Remer, and A. Smirnov, Climatology of dust aerosol size distribution and optical properties derived from remotely sensed data in the solar spectrum, *Journal of Geophysical Research*, 106 (D16), 18,205-18,217, 2001.
- Tegen, I., and I. Fung, Modeling of mineral dust in the atmosphere: sources, transport, and optical thickness, *Journal of Geophysical Research*, 99 (D11), 22,897-22,914, 1994.
- Tegen, I., P. Hollrig, M. Chin, I. Fung, D. Jacob, and J. Penner, Contribution of different aerosol species to the global aerosol extinction optical thickness: Estimates from model results, *Journal of Geophysical Research*, 102 (D20), 23,895-23,915, 1997.

- Tegen, I., and A.A. Lacis, Modeling of particle size distribution and its influence on the radiative properties of mineral dust aerosol, *Journal of Geophysical Research*, 101 (D14), 19,237-19,244, 1996.
- Torres, O., P.K. Bhartia, J.R. Herman, Z. Ahmad, and J.Gleason, Derivation of aerosol properties from satellite measurements of backscattered ultraviolet radiation: Theoretical basis, *Journal of Geophysical Research*, 103 (D14), 17,099-17,110, 1998.
- van de Hulst, H.C., *Light scattering by small particles*, 446 pp., John Wiley & Sons, Inc., New York, 1957.
- van de Hulst, H.C., *Multiple light scattering*, 739 pp., Academic Press, New York, 1980.
- Vermeulen, A., C. Devaux, and M. Herman, Retrieval of scattering and microphysical properties of aerosols from ground-based optical measurements including polarization. I Method, *Applied Optics*, 39 (33), 6207-6220, 2000.
- Vermote, E.F., N. El Saleous, C.O. Justice, Y.J. Kaufman, J.L. Privette, L. Remer, J.C. Roger, and D. Tanré, Atmospheric correction of visible to middle-infrared EOS-MODIS data over land surfaces: Background, operational algorithm and validation, *Journal of Geophysical Research*, 102 (D14), 17,131-17,142, 1997.
- von Hoyningen-Huene, W., and A. Raabe, Maritime and continental air mass differences in optical aerosol extinction data, *Beitr. Phys. Atmosph.*, 60 (1), 81-87, 1987.
- von Hoyningen-Huene, W., and M. Wendisch, Variability of aerosol optical parameters by advective processes, *Atmospheric Environment*, 28, 923-933, 1994.

Wang, M., and H.R. Gordon, Retrieval of the columnar aerosol phase function and single-scattering albedo from sky radiance over the ocean: simulations, *Applied Optics*, 32 (24), 4598-4609, 1993.

Yang, H., H.R. Gordon, and T. Zhang, Island perturbation to the sky radiance over the ocean: simulations, *Applied Optics*, 34 (36), 8354-8362, 1995.

Young, R.W., K.L. Carder, P.R. Betzer, D.K. Costello, R.A. Duce, G.R. Ditullio, N.W.

Tindale, E.A. Laws, M. Uematsu, J.T. Merrill, and R.A. Feely, Atmospheric iron inputs and primary productivity: Phytoplankton responses in the North Pacific, *Global Biogeochemical Cycles*, 5 (2), 1991.

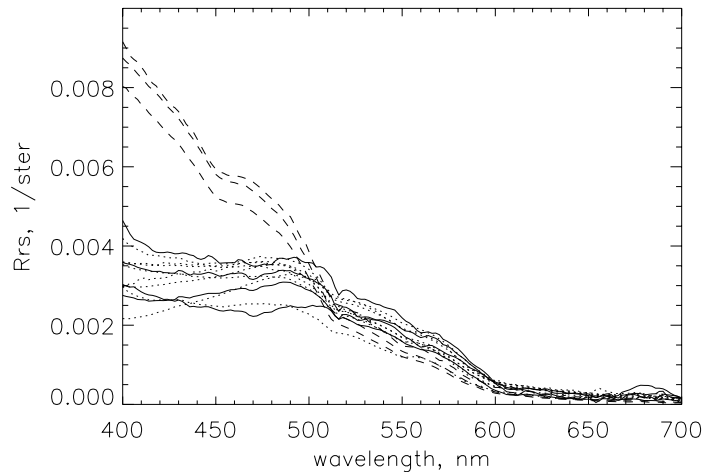
APPENDICES

Appendix A: Clear Water Radiances at Chlorophyll Concentrations < 2.0 mg/m³

In the oligotrophic ocean (found typically between 35 °N and 35 °S), where chlorophyll *a* concentrations are less than 0.25 mg m⁻¹, the remote-sensing reflectance, R_{rs} , and normalized water-leaving radiance, L_{wn} , can be

predicted with an 8% error for wavelengths longer than 500 nm (Gordon and Clark, 1981).

Preliminary data (see diagram) suggest that $R_{rs}(510)$ and $R_{rs}(531)$ can be predicted with about a 13% error for waters with chlorophyll concentrations of up to 2.8 mg m⁻³.



$R_{rs}(\lambda)$ vs. λ for 12 stations in the Gulf of Mexico and near Iceland with chlorophyll concentrations ranging from 0.07 to 2.8 mg m⁻³ (mean 0.58) have a mean \pm standard deviation at 510 and 531 nm of 0.00264 ± 0.00032 and 0.00216 ± 0.00029 , respectively. This yields an estimate of a 12% to 13% error in R_{rs} (and thus in L_{wn}) at 510 or 531 nm (the error is about 17% for 551 nm).

R_{rs} can be converted into L_{wn} via $L_{wn}(\lambda) = R_{rs}(\lambda) F_0(\lambda)$, where F_0 is the incoming extraterrestrial solar irradiance. The mean value of $L_{wn}(551)$ for the data in Fig. 3 is 0.313 mW cm⁻² μ m⁻¹ sr⁻¹, which is nearly the same as the $L_{wn}(550)$ value of 0.30 mW cm⁻² μ m⁻¹ sr⁻¹ that

was used for clear-water atmospheric correction in the processing of CZCS data (Gordon et al., 1983).

We hope to extend the use of “clear-water” radiances to regions with chlorophyll concentrations as high as 0.5-1.0 mg/m³. For major dust outbreaks where the major flux of iron to the ocean might be expected, $L_{as}(531)$ will be far greater than the increase in uncertainty in $L_w(531)$.

APPENDIX B

Columnar aerosol single-scattering albedo and phase function retrieved from sky radiance over the ocean: Measurements of Saharan dust

Christopher Cattrall

College of Marine Science, University of South Florida, St. Petersburg, Florida

Kendall L. Carder

College of Marine Science, University of South Florida, St. Petersburg, Florida

Howard R. Gordon

Department of Physics, University of Miami, Coral Gables, Florida

Journal of Geophysical Research (Atmospheres)

Corresponding Author: Christopher Cattrall

College of Marine Science, University of South Florida

St. Petersburg FL 33701-5016 USA

(tel.) 727-553-3952 (FAX) 727-553-1189

email: chris@monty.marine.usf.edu

Abstract.

The single-scattering albedo and phase function of African mineral dust are retrieved at fourteen wavelengths across the visible spectrum from ground-based measurements of the aerosol optical thickness and the sky radiance taken in the solar principal plane. The retrieval algorithm employs the radiative transfer equation to solve by iteration for these properties that best reproduce the observed sky radiance and is therefore independent of particle shape. The single-scattering albedo displays a spectral shape expected of iron-bearing minerals but is much higher than climate models have assumed, indicating windblown mineral dust cools Earth more than is generally believed. The estimated error in the retrieved single-scattering albedo is less than 0.02 due to the precision of the solar-reflectance-based calibration of the radiometer. The phase function retrieved at 860 nm is robust under simulations of expected experimental errors and may be used to characterize aerosol scattering at the directly measured scattering angles (i.e., $\Theta \leq 155^\circ$), but the phase function retrieved at 443 nm is too sensitive to such errors to confidently describe the angular scattering at blue wavelengths. This method may be applied to any combination of airborne and ground-based measurements over the ocean and can complement more involved ground-based retrievals through its insensitivity to particle shape and ability to retrieve aerosol properties at relatively small aerosol optical depths.

1. Introduction

Tropospheric aerosols represent perhaps the greatest uncertainty in studies of climate change [Charlson *et al.*, 1992; Hansen *et al.*, 2000]. Aerosols influence the radiation balance of the earth directly by interacting with solar and terrestrial radiation and indirectly by altering cloud properties and amount [Haywood and Boucher, 2001]. Their enormous heterogeneity dictates that the geographical and seasonal distribution of aerosol properties and concentration must be known before accurate estimates of the direct forcing by aerosol may be made [Hansen *et al.*, 1995]. Observations from space

alone cannot yet furnish the complete set of required aerosol parameters [Tanré *et al.*, 1996], such that remote sensing of both aerosol and Earth's ecosystems presently depend on aerosol models to determine many surface and atmospheric properties [Gordon, 1997; Kahn *et al.*, 1998; Kaufman *et al.*, 2001; Mishchenko *et al.*, 1999; Torres *et al.*, 1998; Vermote *et al.*, 1997]. In this respect, ground-based radiometric measurements are very useful because the direct solar beam and intensity of light about the sky contain sufficient information to derive the complete set of aerosol radiative parameters: optical thickness $\tau(\lambda)$; single-scattering albedo $\omega_0(\lambda)$, the ratio of scattering to extinction (absorption + scattering); and phase function $P(\Theta, \lambda)$, the angular distribution of scattered light [Dubovik and King, 2000; Wang and Gordon, 1993], where λ represents wavelength. Further, since the direct forcing is very sensitive to aerosol absorption [Hansen *et al.*, 1997] and the aerosol single-scattering albedo is difficult to measure from space [Kaufman *et al.*, 1997], accurate ground-based determinations of ω_0 for each aerosol species are a prerequisite to improved climate assessments.

Mineral dust is responsible for roughly one-third of global aerosol extinction optical thickness [Tegen *et al.*, 1997] and absorbs significantly in the blue and ultraviolet wavelengths due to iron oxide impurities [Claquin *et al.*, 1999; Sokolik and Toon, 1999]. A consensus on the magnitude of the absorption has proved elusive, with laboratory measurements placing ω_0 at $0.5\mu\text{m}$ between 0.63 and 0.87 [see Sokolik and Toon, 1996] and broadband flux measurements placing ω_0 at 0.95 [Fouquart *et al.*, 1986]. Remote sensing has evolved to become a powerful method for characterizing the suspended aerosol [Dubovik and King, 2000; Kaufman *et al.*, 2001; Moulin *et al.*, 2001a], such that a clearer picture of the optical properties of each aerosol species is emerging [Dubovik *et al.*, 2002]. However, spherical particles are usually assumed when interpreting scattered radiance, yet nonspherical particles such as mineral dust produce angular scattering patterns distinctly different from area-equivalent spheres [Mishchenko *et al.*, 1997]. Remote sensing methods that derive the aerosol single-scattering albedo

independent of particle shape are therefore useful to climate studies and remote sensing of the environment.

Aerosol information can be extracted from sky radiance using the radiative transfer equation to solve directly for $\omega_0(\lambda)$ and $P(\Theta, \lambda)$ of the columnar aerosol [Wang and Gordon, 1993]. The method retrieves these properties independent of aerosol shape at any measured wavelength outside of gaseous absorption lines. In this study, we apply the Wang-Gordon algorithm to measurements of sky radiance taken during two strong mineral dust events. The broad spectral range of the radiometer (380-870 nm) affords characterization of both the magnitude and spectral behaviour of ω_0 of windblown mineral dust.

2. Methods

2.1 Definitions

Normalized downward radiance, ρ , is defined as

$$\rho(\lambda) = \frac{\pi L(\lambda)}{\mu_o F_o(\lambda)}, \quad (1)$$

where L is the downward radiance at the bottom of the atmosphere, F_o the extraterrestrial solar irradiance, and μ_o the cosine of the solar zenith angle θ_o . In this paper, the term radiance means normalized radiance, not absolute radiance. The algorithm uses normalized radiance; since the solar-reflectance-based calibration is independent of F_o , [Biggar *et al.*, 1994; Cattrall *et al.*, Solar-reflectance-based calibration of spectral radiometers, submitted to *Geophysical Research Letters*, 2002], the extraterrestrial irradiance need never be known, which reduces uncertainty in the measured sky radiance to 2.5% [Cattrall, 2002].

The total radiance received by a ground-based sensor can be written as [Wang and Gordon, 1993]

$$\rho_t(\lambda) = \rho_r(\lambda)e^{-\tau_a(\lambda)/\mu} + \rho_a(\lambda)e^{-\tau_r(\lambda)/\mu_0} + \rho_{ra}(\lambda), \quad (2)$$

where τ_a and τ_r represent the aerosol and molecular optical depths, respectively; μ , the cosine of the viewing angle; ρ_r , the molecular radiance in an atmosphere without aerosol; ρ_a , the aerosol radiance in an atmosphere without air; and ρ_{ra} is an interaction term which gives the correct total radiance ρ_t . Equation 2 is useful for interpreting the results of the sensitivity study (Section 3.3).

2.2 Sampling location

All radiometric data were taken during the months of July and August 1998 at Ft. Jefferson, Dry Tortugas (24° 37.7' N, 82° 52.5' W), an island site approximately 70 miles west of Key West, Florida (Fig. B1). The Dry Tortugas are free of most anthropogenic influences and southerly enough to experience frequent passage of Saharan dust during summer months [*Prospero*, 1981; *Prospero et al.*, 2001].

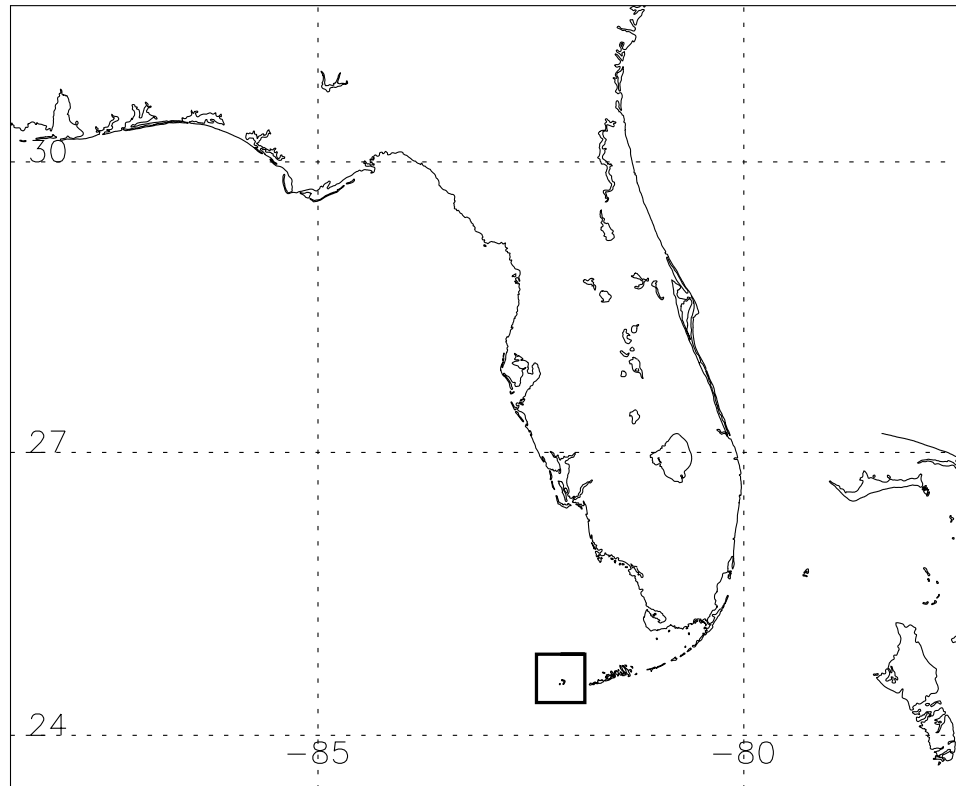


Figure B1. Sampling location. Dry Tortugas are outlined by the box.

2.3 Apparatus and procedure

Measurements were taken when the sky was cloudless and hazy. These conditions always occurred following passage of thunderstorms, as would be expected of dust pulses preceded by easterly wave disturbances [Karyampudi and Carlson, 1988] and suppressed convection due to the warm Saharan air [Carlson and Prospero, 1972].

Sky radiance was collected in the solar principal plane with a portable 512-channel spectrometer (FWHM 2.3 nm, 3.2° full field-of-view), constructed at the USF Ocean Optics Laboratories. Azimuth

viewing angle was measured with a gimballed KVH Industries C100 compass engine ($\pm 1^\circ$) and zenith viewing angles with a digital Mitsuyo clinometer ($\pm 0.1^\circ$). Solar zenith angle during measurement was between 65 and 70° . The maximum measured scattering angle Θ_{\max} , is $\Theta_{\max} \leq \theta_o + \pi/2$, where

$$\cos \Theta = \cos \theta_o \cos \theta + \sin \theta_o \sin \theta \cos(\phi - \phi_o).$$

θ represents the viewing zenith angle, and ϕ and ϕ_o the viewing and solar azimuth angles, respectively. In practice, data was collected in intervals of $\sim 2^\circ$ in the solar aureole, increasing to 10° at side-scattering angles, and reduced to 5° when approaching the opposite horizon. The range of measured scattering angles was approximately 3° - 155° . A collection sequence comprised roughly 25 scan sets with each set containing 3 spectral scans. Instantaneous aerosol optical depths were continuously measured by two calibrated 10-channel Reagan solar radiometers [Ehsani, 1992]. A Campbell Scientific meteorological station recorded ambient relative humidity, temperature and barometric pressure.

2.4 Data processing

Atmospheric homogeneity was established by examining the stability of instantaneous optical depths measured by the Reagan radiometers and the symmetry of aureole radiance collected by an AERONET instrument also operating in the Dry Tortugas. The sky radiance and optical depth data are publicly available from this network [Holben *et al.*, 1998]. The presence of dust was confirmed by optical characterization, back-trajectory analysis, and concurrent airborne mineral dust concentrations (see Section 3.2). Means of the instantaneous aerosol optical depths gave $\tau_a(\lambda)$ to be used in the algorithm.

2.5 Algorithm description

2.5.1 Principle of the method

The radiative transfer code has been used previously to examine the accuracy of atmospheric correction algorithms [Gordon and Wang, 1992a,b]. It employs the successive-order-of-scattering method [van de Hulst, 1980] to compute the upward radiance at the top of the atmosphere and the

downward radiance at the bottom of the atmosphere. The atmosphere is plane parallel, bounded below by a choice of completely absorbing or Fresnel-reflecting ocean, with an aerosol layer homogeneously mixed from the surface to a specified height embedded within a molecular scattering atmosphere.

The algorithm determines by iteration the aerosol single-scattering albedo and phase function which best produce the measured sky radiance. To begin, an initial guess of $\omega_o(\lambda)P(\Theta)$ and the measured $\tau_a(\lambda)$ are inserted into the radiative transfer equation (RTE), and the downward radiance at the bottom of the atmosphere computed. Differences between the computed and measured sky radiance at each angle are used to calculate a new phase function and albedo for the next iteration. Using single-scattering as a guide, this difference, $\Delta[\omega_o P]$, is given by

$$\Delta[\omega_o(\lambda)P(\Theta, \lambda)] = \omega_o(\lambda)P(\Theta, \lambda)^{(m)} \left\{ \frac{\rho_t(\lambda)^{(c)} - \rho_t(\lambda)^{(m)}}{\rho_t(\lambda)^{(m)} - \rho_r(\lambda)^{(c)} e^{-\tau_a(\lambda)/\mu}} \right\}, \quad (3)$$

where the superscripts c, m represent the computed and measured quantities, respectively. Since the phase function cannot be measured for scattering angles greater than Θ_{\max} , $P(\Theta > \Theta_{\max})$ is assigned the value of $P(\Theta_{\max})$ at each iteration. This process is repeated until convergence is achieved to within a specified tolerance at all measured scattering angles.

2.5.2 Inversion algorithm

The algorithm proceeds in the steps outlined below:

- (1) A two-term Henyey-Greenstein phase function with $\omega_o = 1$ is used for initial estimates of $\omega_o(\lambda) \cdot P(\Theta, \lambda)$
- (2) $\tau_a(\lambda)$, and $\omega_o(\lambda) \cdot P(\Theta, \lambda)$ are inserted into the RTE to calculate the total sky reflectance $\rho_t^{(c)}(\lambda, \theta, \phi)$
- (3) New values of $\omega_o(\lambda) \cdot P(\Theta, \lambda)$ are calculated up to Θ_{\max} by

$$[\omega_o(\lambda) \cdot P(\Theta, \lambda)]_{new} = [\omega_o(\lambda) \cdot P(\Theta, \lambda)]_{old} * \left\{ 1 - \frac{1}{2} \Delta[\omega_o(\lambda) \cdot P(\Theta, \lambda)] \right\}$$

A value of 1/2 is used to avoid instability during iteration.

- (4) Values of $P(\Theta, \lambda)$ for $\Theta > \Theta_{max}$ are assigned to equal $P(\Theta_{max})$
- (5) Steps (3) and (4) are repeated until convergence is achieved to within a specified tolerance (e.g., 0.2% of the radiance at every scattering angle). This usually required 8-12 iterations.

2.5.3 Retrieval of $\omega_o(\lambda)$ and $P(\Theta)$

The product $\omega_o P(\Theta)$ is never separated in the computations. Once convergence is achieved, the terms are separated using the normalization condition of the phase function,

$$\frac{1}{2} \int_0^\pi \sin \Theta \cdot P(\Theta) \cdot d\Theta = 1, \text{ i.e., } (4)$$

$$\omega_o(\lambda) = \frac{1}{2} \int_0^\pi [\omega_o(\lambda) \cdot P(\Theta, \lambda)] \cdot \sin \Theta \cdot d\Theta. \quad (5)$$

Note the angular behaviour of $P(\Theta)\sin\Theta$ means ω_o is overwhelmingly determined by radiance scattered in the forward direction.

2.5.4 Validity of retrieved quantities

The algorithm has been tested with sky radiance data computed by exact scalar radiative transfer codes, retrieving the single-scattering albedo and phase function with virtually no error in error-free simulations [Wang and Gordon, 1993]. Simulations also show the plane parallel assumption and use of scalar (rather than vector) computations cause negligible error in the retrievals [Gordon and Zhang, 1996]. The method by which to extrapolate the integrand (see Eq. 5) between 0° and the minimum

measured scattering angle does not significantly affect the value of the integral [*Wang and Gordon, 1993*].

The effects of expected experimental errors are investigated by applying simulated error to the measured field data and observing the changes in the retrieved quantities (see Section 3.3). The effect of a likely background aerosol presence upon the retrievals is also explored.

3. Results

3.1 Summary of the results

Two major dust events were sampled (July 23-24; 27-29). The retrieved optical properties varied little, allowing mean optical properties to be constructed.

The single-scattering albedo is near unity at red wavelengths, and decreases with decreasing wavelength (Fig. B2). This spectral behaviour is consistent with iron-bearing minerals such as Saharan dust [*Sokolik and Toon, 1999*]. However, the absorption is significantly less than models commonly computed from laboratory measurements of the complex refractive index of Saharan dust [*Patterson, 1977*].

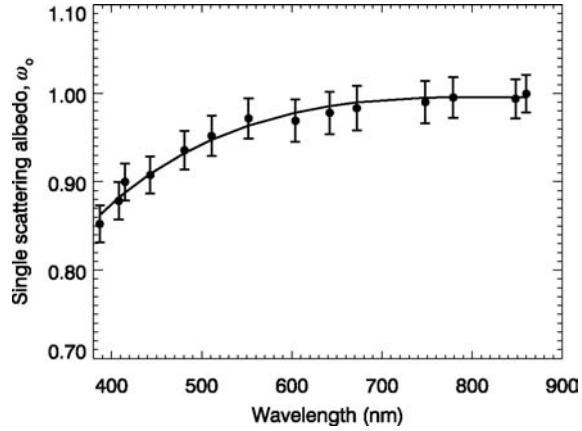


Figure B2. Mean retrieved single-scattering albedo, $\omega_0(\lambda)$. Solid line represents the best logsquare fit to the data (3-term polynomial). The error bars represent the uncertainties computed by the sensitivity study (Section 3.3)

The scattering phase functions are also temporally consistent (Fig. B3). Retrievals at 860 and 443 nm on three days are shown to illustrate the agreement.

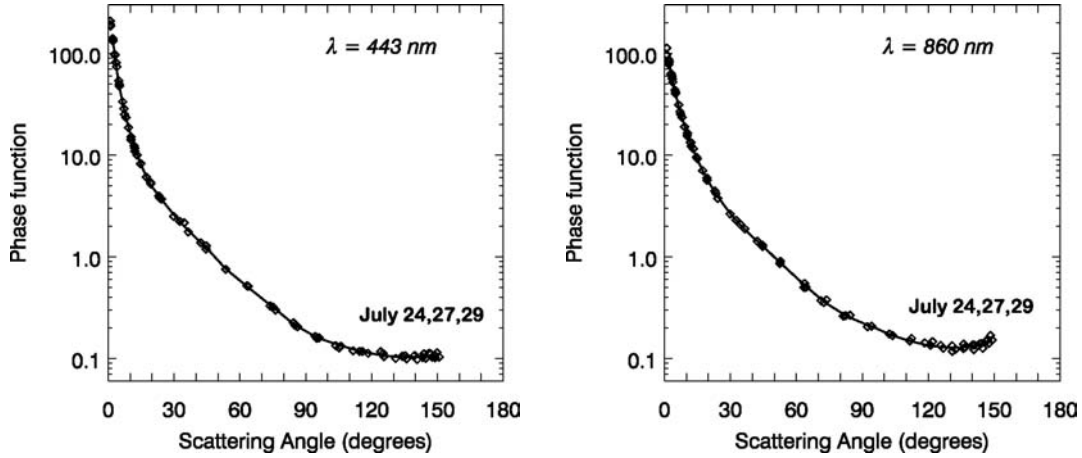


Figure B3. Retrieved scattering phase functions. Results of 3 sky radiance collections. Solid line represents best fit to data. The open diamonds represent data points of the sky measurements

3.2 Detailed results

3.2.1 Airmass identification

Daily means of the aerosol optical depth measured at 500 nm throughout the summer by the AERONET instrument in the Dry Tortugas show periods of strong atmospheric turbidity (Fig. B4a). Fires in north Florida contributed to aerosol loading in late June but burnt out in early to mid-July. Daily aerosol statistics for Miami (courtesy J. Prospero, University of Miami) display elevated nitrate concentrations in the aerosol during June and early July (Fig. B4b), indicating the presence of biomass burning or anthropogenic pollution [Prospero, 1999]. Low nitrate and high mineral dust concentrations during mid and late July show that mineral dust was the dominant aerosol component during the

measurement period at Ft. Jefferson (July 23-29). The dust events are clearly observed in both the AERONET optical depths and the mineral dust concentrations in Miami (Fig. B4).

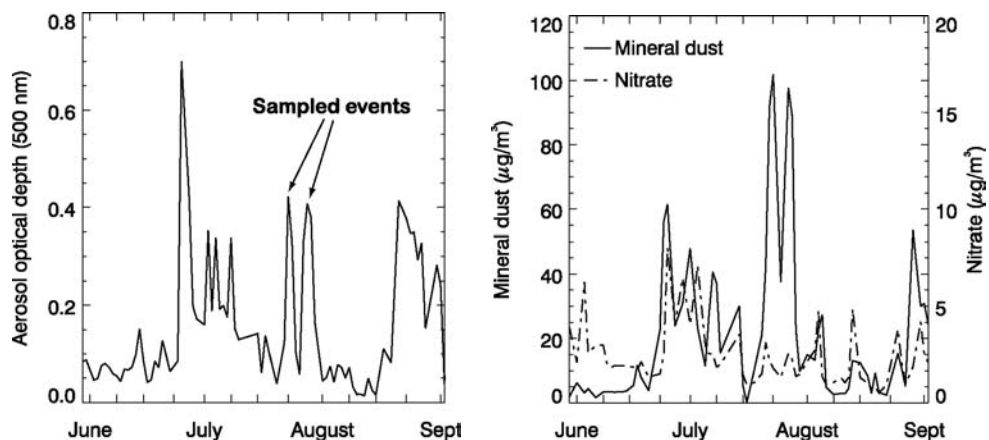


Figure B4. Atmospheric conditions, summer 1998. *Left panel.* AERONET daily mean aerosol optical depth (500 nm), June – Sept, 1998. *Right panel.* Mineral dust and nitrate concentrations at Miami, June – Sept, 1998. (courtesy J. Prospero, U. Miami).

3.2.2 Trajectory analysis

Air mass trajectories were computed for the two dust events using the HYSPLIT (Hybrid Single Particle Lagrangian Integrated Trajectory) code available from the Air Resources Laboratory of the National Oceanic and Atmospheric Administration (NOAA ARL). Isentropic trajectories of 96 hours were calculated at 1800 UTC for 500, 1000, and 3000m. The air parcels over the Dry Tortugas during the measurement period consistently arrived from the easterly or southeasterly sectors (Fig. B5), a common characteristic of winds over south Florida in the summer [Henry *et al.*, 1994], and in accord with winds

associated with high dust concentrations observed every year in Bermuda, Barbados and Miami [Arimoto *et al.*, 1995; Prospero, 1999].

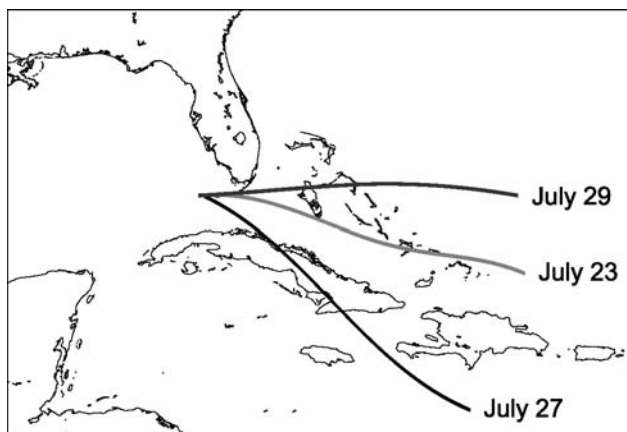


Figure B5. Trajectory analysis (HYSPLIT)

5-day back trajectories for air parcels arriving at the Dry Tortugas, Florida Keys, during the field experiment.

3.2.3 Satellite imagery

Five-day composites (pentads) of second-generation AVHRR images [Stowe *et al.*, 1997] clearly show the emergence of the dust plume from the west coast of Africa in mid-July (Fig. B6a) and westward progression across the Atlantic (Figs. B6b,c) to blanket the southern tip of Florida during the period in which the radiometric measurements were taken (July 23-29). The transit time of 5-7 days is typical for a Saharan dust event [Savoie and Prospero, 1977]. Identical patterns of dust advection across the Atlantic Ocean are frequently observed from space [Chiapello *et al.*, 1999; Herman *et al.*, 1997; Husar *et al.*, 1997; Ott *et al.*, 1991].

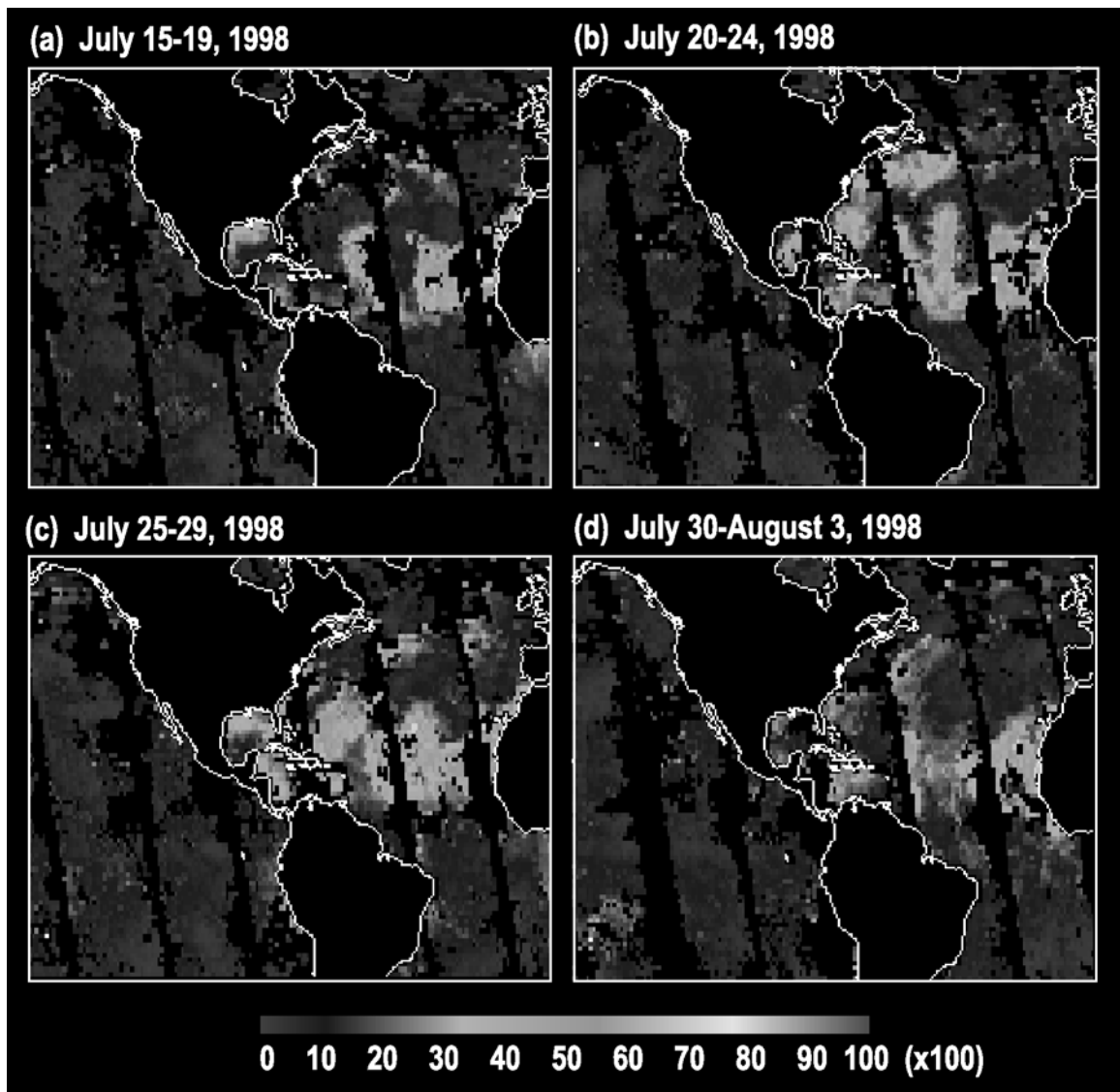


Figure B6. 5-day composites of aerosol optical depth (AOD) at 0.63 μm derived from NOAA Advanced Very High Resolution Radiometer (AVHRR) satellite using second generation algorithm (*images courtesy NOAA Active Archive*).

3.2.3 Optical characterization

Clean maritime atmospheres usually possess aerosol optical depths at 550 nm (τ_{550}) less than 0.15, while those for Saharan dust over the tropical North Atlantic are often between 0.3 and 0.5 [Korotaev *et al.*, 1993; Reddy *et al.*, 1990]. Aerosol optical depths measured during the dust events were typically greater than 0.4. Under clean maritime conditions, τ_{550} was approximately 0.1 (Fig. B7).

Aerosol optical depth can be related to wavelength by,

$$\tau_a(\lambda) = \beta \cdot \lambda^{-\alpha},$$

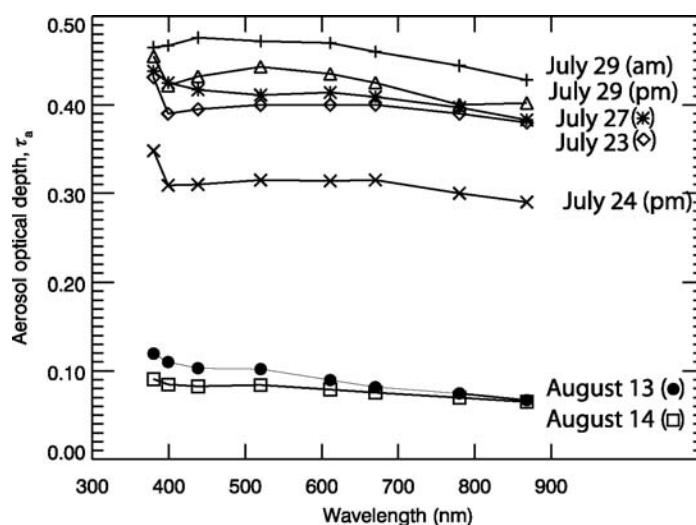


Figure B7. Aerosol optical depths during the Dry Tortugas experiment

where α is the Angstrom exponent [Ångström, 1964]. Exponents of mineral dust are often small due to the larger, coarse-mode particles [Tanré *et al.*, 1988] and can be negative over some spectral regions [Carlson and Caverly, 1977]. Angstrom exponents are usually less than 0.5 for pure Saharan dust [Eck *et al.*, 1999; Reddy *et al.*, 1990; Smirnov *et al.*, 1998; Tanré *et al.*, 1988]. In contrast, values for smaller maritime aerosols generally fall between 1 and 2 [Ångström, 1964; Hoppel *et al.*, 1990; Reddy *et al.*, 1990; von Hoyningen-Huene and Wendisch, 1994]. Optical depths and Angstrom

exponents observed during the experiment are summarized in Table B1. The range of measured Angstrom exponents and aerosol optical depths indicate that mineral dust dominated the optical properties of the columnar aerosol during the field campaign, although a background “marine” aerosol is always present.

Table B1. Angstrom exponents and optical depths during sky measurements

Date	$\alpha = \Delta \ln \tau / \Delta \ln \lambda$	$\tau_a(550)$
23-Jul	0.08	0.45
24-Jul		
morning	0.12	0.39
evening	0.18	0.31
27-Jul	0.15	0.41
29-Jul	0.20	0.45
13-Aug	0.85	0.09
14-Aug	0.70	0.10

3.3 Sensitivity study

Wang and Gordon (1993) provided a sensitivity study of the algorithm using simulated data. Here, a sensitivity study is performed on the sky radiance measurements themselves to test the stability of the retrievals. Specifically, the effects of error in calibration, optical depth, observation angle, ground reflectance and the assumption of vertical structure are explored. The relatively low optical depth ($\tau_{550} = 0.32$) on the morning of July 24 provides the most severe test of the algorithm. This owes to the fact that

the absolute error in the aerosol contribution is approximately the same as in ρ_a , so the smaller τ_a is, the larger the relative error in the aerosol contribution will be. Mean results for sensitivity analyses performed on the measurements taken July 24 and July 27 are given at the end of this section, and represent the uncertainty in the mean retrieved aerosol optical properties.

We effect the sensitivity study by using the algorithm to retrieve the phase function and single-scattering albedo using the measured input data, and then examine the retrievals as the input data is varied to reflect calibration error, etc. The average difference between the retrieved phase functions, δ_{ave} , displayed in the next several figures is defined as

$$\delta_{ave} = \frac{1}{N} \sum_{i=1}^N \left| \frac{P_o(\Theta_i) - P'(\Theta_i)}{P_o(\Theta_i)} \right| \times 100 \%,$$

where $P_o(\Theta)$ is the phase function derived with the measured input data; $P'(\Theta)$, the phase function retrieved from sky radiance data which includes the simulated error; and N , the number of measured scattering angles. The sensitivity study described in Figures B8-B11 involves adjustments to the input data applied to the July 24 morning measurements ($\tau_{550} = 0.32$)

3.3.1 Spectrometer calibration

Figure B8 shows the case of a radiometric calibration error ($\Delta L = \pm 2.5\%$). Most of the simulated error appears in the single-scattering albedo since the retrieved albedo is influenced most greatly by the near-forward scattered radiance (Eq. 5). The greater contribution from Rayleigh scattering at shorter wavelengths causes the retrieved albedo to be more sensitive to calibration error at 443 nm than at 860 nm. The new albedo causes differences in the path radiance, for which the algorithm compensates by altering the phase function. Hence, differences between the retrieved phase functions increase with scattering angle and decreasing wavelength (i.e., greater multiple scattering).

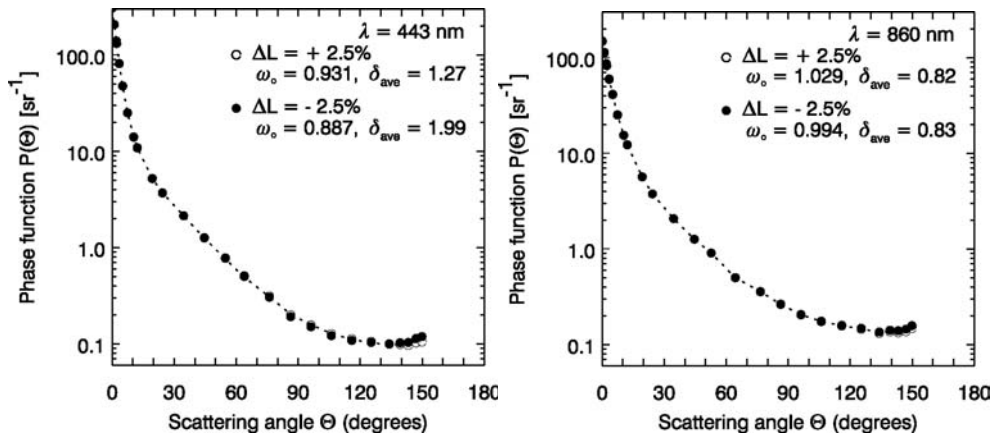


Figure B8. Retrieved ω_0 and $P(\Theta)$ for $\Delta L = \pm 2.5\%$

The retrieved single-scattering albedos without simulated error are

$\omega_0(860) = 1.01$ and $\omega_0(443) = 0.908$. **Note:** The retrieved $\omega_0(860)$ is

greater than unity for this day, but the mean $\omega_0(860)$ is 1.00. The dashed

line is the $P(\Theta)$ retrieval without simulated error. Note that δ_{ave} is mean error in percent (see text).

3.3.2 Optical depth

Figure B9 shows the case of an error in the measured aerosol optical thickness ($\Delta\tau=\pm 10\%$ or, here, 0.032). At 860 nm much of the simulated error is reflected in the single-scattering albedo with the remaining differences between path radiance seen in the phase function. At 443 nm, where molecular

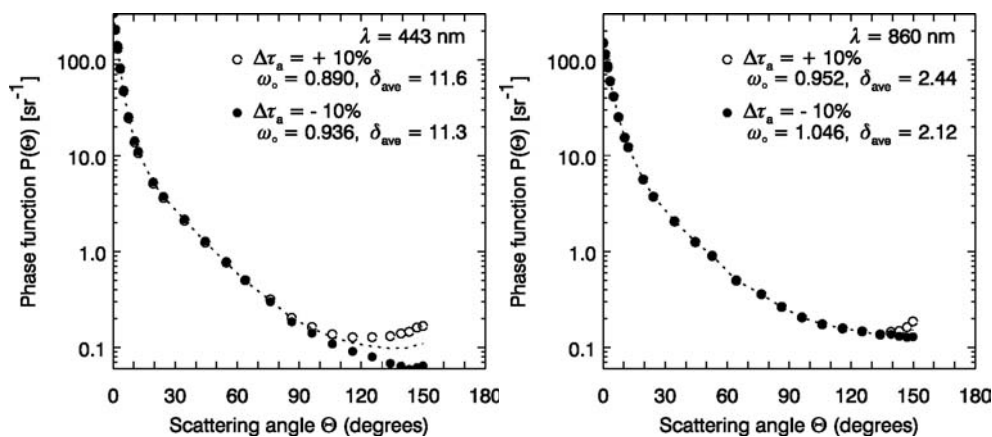


Figure B9. Retrieved ω_o and $P(\Theta)$, $\Delta\tau_a = \pm 10\%$ scattering is much greater, the effects of an incorrect optical depth are mitigated by the corresponding change in attenuation of the molecular radiance (see Eq. 2). Differences in the retrieved single-scattering albedo are thus smaller at shorter wavelengths. The retrieved phase functions, however, are very different at backscattering angles at 443 nm because even small errors in the single-scattering albedo lead to significant differences in the path radiance when the pathlength through the atmosphere is great.

3.3.3 Viewing angles

Figure B10 shows the case of an incorrect viewing zenith angle ($\Delta\theta = \pm 0.2^\circ$). An error in the zenith angle shifts the $\omega_o P(\Theta)$ integrand, altering the value of the integral (Eq. 5). Differences in single-scattering albedo, although slight, again affect the path radiance and thus the retrieved phase functions, where atmospheric pathlength is large.

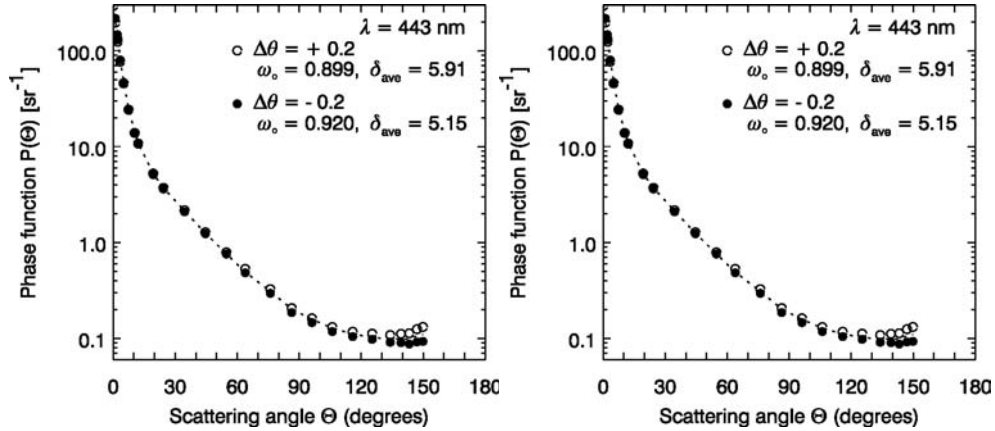


Figure B10. Retrieved ω_0 and $P(\Theta)$, $\Delta\theta = \pm 0.2^\circ$

3.3.4 Aerosol vertical structure

If a different vertical structure is used in the retrieval, the single-scattering albedo remains virtually unchanged (Fig. B11) since aerosol vertical distribution negligibly affects radiance in the solar aureole. At larger scattering angles, the vertical distribution of an absorbing aerosol can influence the path radiance at 443 nm. For example, if aerosol height is underestimated (e.g., 2 km is assumed in the retrieval rather than 4 km), light attenuation before the event of scattering is overestimated at side-scattering angles, and the phase function therefore underestimated. At back-scattering angles, multiple interactions compound the inaccuracies in the phase function at side-scattering angles, such that the algorithm compensates by overestimating the phase function at back-scattering angles.

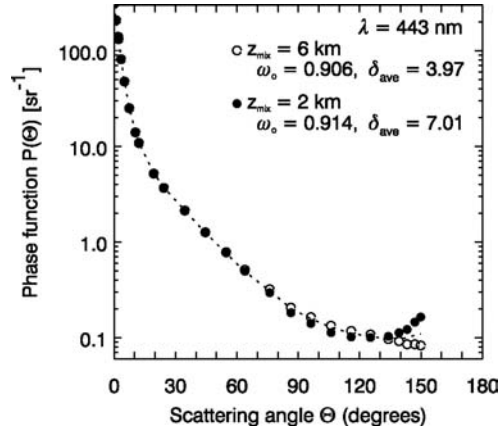


Figure B11. Retrieved ω_o and $P(\Theta)$ with different vertical distributions.

The retrieved single-scattering albedo without error is $\omega_o(443) = 0.908$.

3.3.5 Extrapolation of $P(\Theta)$, $\Theta > \Theta_{max}$

We investigated the effect of assuming a constant phase function at angles greater than the maximum measured angle, Θ_{max} , by linearly extrapolating the last 5 phase function points. Figure B3 displays the typical shape of the retrieved phase functions. The greatest difference at 860 nm over all days was 8% at the greatest scattering angle, but differences of 4% were much more common (Fig. B12). The extrapolation of 443 nm was almost flat, resulting in very little change in the retrieved phase function. Thus, the shape of the phase function has some influence on these results. Nonspherical particles display rather flat side- and back-scattering [Mishchenko *et al.*, 1997]; retrievals in the presence of mineral dust are therefore much less affected by the assumed shape of $P(\Theta) > \Theta_{max}$ than, say, a maritime aerosol possessing strong backscattering. The assumed shape of the phase function at these large scattering angles has a negligible influence on the retrieved ω_o (~ 0.0001).

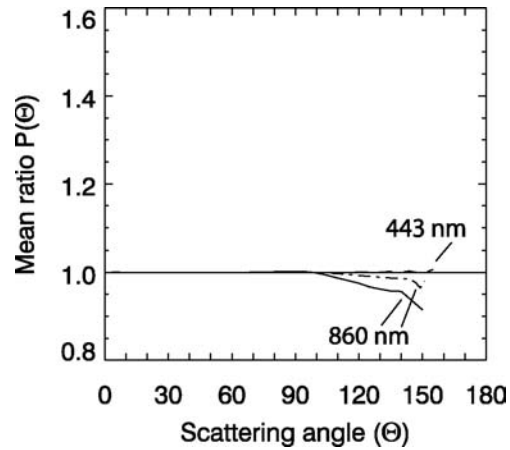


Figure B12. Effect of assumed phase function, $\Theta > \Theta_{\max}$. Ratio of phase function obtained by linear extrapolation of last 5 points to phase function using original assumption of $P(\Theta) = P(\Theta_{\max})$. Uppermost curve of 860 nm is July 27, lower curve is for July 24.

3.3.6 Other considerations

Computations performed with MODTRAN4 [Acharya *et al.*, 1998] using a completely absorbing surface and one with the reflectance properties of shallow water show the total sky radiance is negligibly affected at all angles (mean deviation 0.7%). The measurements in the Dry Tortugas were performed facing open water, in such a manner as to mitigate the island effect [Yang *et al.*, 1995]. Furthermore, Figure B5 from Yang *et al.* (1995) shows the effect for an island the size of Garden Key ($r \sim 0.3$ km) to be almost zero under similar atmospheric conditions. Thus, water-leaving radiance and ground reflectance causes negligible error in the retrievals.

3.3.7 Summary

The results of these simulations – performed on real field data – agree with previous theoretical studies of error in similar ground-based retrievals [*Devaux et al.*, 1998; *Vermeulen et al.*, 2000; *Wang and Gordon*, 1993]. Specifically, an overestimate of sky radiance leads to an overestimate of aerosol single-scattering albedo, as does an underestimation of aerosol optical depth. The reverse cases are also true. These relationships are not linear, i.e., a 2.5% error in radiance or optical depth does not cause a 2.5% error in $\omega_0(\lambda)$ since multiple scattering can be a significant portion of the signal. Errors in optical depth are further mitigated by differences in attenuation of the scattered light. Errors in viewing angle contribute less than those of optical depth and calibration to the total uncertainty in $\omega_0(\lambda)$.

Table B2. Estimated uncertainty in $\omega_0(\lambda)$

Error (%) in ω_0			
Situation	443 nm	552 nm	860 nm
$\Delta L = +2.5\%$	+1.7	+1.3	+1.0
$\Delta L = -2.5\%$	-2.1	-2.0	-1.9
$\Delta\tau_a = +0.03$	-0.6	-1.3	-2.2
$\Delta\tau_a = -0.03$	+0.7	+1.4	+1.9
$\Delta\theta_{\text{view}} = +0.2^\circ$	-0.8	-1.0	-1.2
$\Delta\theta_{\text{view}} = -0.2^\circ$	+0.7	+0.7	+0.5
$Z_{\text{mix}} = 6 \text{ km}$	+0.1	0.0	0.0
$Z_{\text{mix}} = 2 \text{ km}$	-0.2	0.0	0.0
ω_0	0.908	0.972	1.000
Uncertainty			
Statistical	0.013	0.017	0.012
Experimental	0.020	0.018	0.018
Estimated $\Delta\omega_0$	0.020	0.024	0.022

Total experimental uncertainty computed by $\Delta\omega_0/\omega_0 = (\Delta L^2 + \Delta\tau^2 + \Delta\theta^2 + \Delta z^2)^{1/2}$, where the error caused by each situation is the mean of the positive and negative case. For example, mean error resulting from uncertainty in radiance at 443 nm = 1.9%. Total uncertainty computed by root-mean-square of statistical and experimental uncertainty.

3.4 Uncertainty in $\omega_0(\lambda)$ and $P(\Theta)$ retrievals

The uncertainty in the mean single-scattering albedo and phase function are obtained by applying error to sky radiance data from July 24 and 27, and represent mean atmospheric conditions during the two dust events. Table 2 displays the uncertainty in the single-scattering albedo. Differences between the phase functions retrieved under normal conditions and with simulated error are shown in Figure B13. The phase function retrieved at 860 nm is very robust under all expected errors, indicating it is accurately retrieved at this wavelength. At 443 nm the combined effects of a more sharply peaked phase function, greater absorption, and multiple interactions, cause significant uncertainty in the retrieved phase function at larger scattering angles.

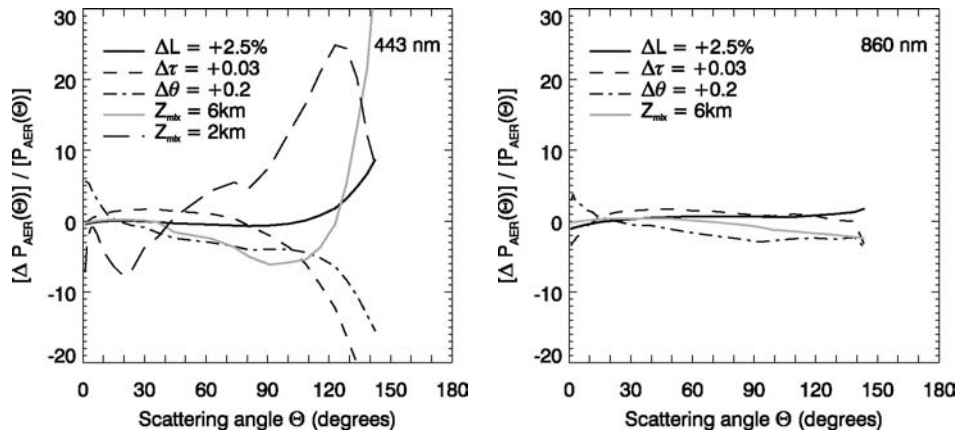


Figure B13. Relative difference in retrieved $P(\Theta)$. The simulated errors are those used to compute the error in the retrieved single-scattering albedo.

3.5 Effect of background aerosol

Although mineral dust dominated the atmospheric aerosol burden during the field experiment, the unavoidable presence of a background “marine” aerosol will somewhat influence the retrieved optical properties. To gain insight into how the retrieved single-scattering albedo may have been affected, we simulated sky radiance using an atmosphere containing a mixture of mineral dust and background maritime aerosol and retrieved the columnar aerosol optical properties using the Wang-Gordon algorithm. The background model we employed was a coastal aerosol introduced by *Gordon and Wang* [1994] to describe the aerosol over the ocean near the coast; it is constructed from the tropospheric and oceanic components of *Shettle and Fenn* [1979] using a number fraction of 99.5% and 0.5%, respectively. Both components are hygroscopic, such that the optical properties of the model change with relative humidity. We selected a relative humidity of 70% because the C70 model best matched the Angstrom exponents observed in the Dry Tortugas under dust-free conditions (see Table 1). In the simulations, the coastal aerosol is homogeneously mixed from 0 to 1 km, with $\tau_{550} = 0.05$, and three dust models of varying absorption (BDW1, BDW2 and BDW3 from *Moulin et al.*, 2001) homogeneously mixed between 1 and 4 km, with $\tau_{550} = 0.35$. A background aerosol optical depth of 0.05 is consistent with our observations in dust-free conditions (Fig. B7) and values historically measured by AERONET in the Dry Tortugas in clear atmospheres (not shown). To maximize the impact of the boundary-layer aerosol, we set the C70 model's ω_0 to unity at all wavelengths (the actual values of ω_0 are 0.9795, 0.9804, and 0.9820, at 412, 443, and 510 nm, respectively).

Table 3. Effect of background aerosol upon retrieved ω_0

	412 nm				€	443 nm				€	510 nm			
	ω_0	$\Delta\omega_0$	ω_0'	$\Delta\omega_0'$		ω_0	$\Delta\omega_0$	ω_0'	$\Delta\omega_0'$		ω_0	$\Delta\omega_0$	ω_0'	$\Delta\omega_0'$
BDW1	0.917 (.900)	0.017	0.914	0.003		0.949 (.939)	0.010	0.947	0.002		0.966 (.960)	0.006	0.965	0.001
BDW2	0.896 (.873)	0.023	0.890	0.006		0.924 (.911)	0.013	0.923	0.001		0.938 (.933)	0.005	0.941	-0.003
BDW3	0.877 (.847)	0.030	0.868	0.009		0.901 (.884)	0.017	0.900	0.001		0.912 (.907)	0.005	0.919	-0.007

Single-scattering albedo (ω_0) retrieved when coastal aerosol (C70; $\omega_0=1.00$) is present in background concentrations. ω_0 of the pure dust models (BDW) are given in parentheses. In the simulations, $\tau_{550} = 0.05$ and 0.35 for the coastal and dust aerosol, respectively. The weighted columnar aerosol single-scattering albedo (ω_0') is computed from the fractional contribution by each species to total aerosol optical depth at each wavelength. Angstrom exponents of aerosol models are 0.62 (C70), 0.22 (BDW1), 0.20 (BDW2), and 0.18 (BDW3).

The simulations show the retrieved albedo is certainly increased by the presence of a non-absorbing aerosol, and that the Wang-Gordon algorithm retrieves the weighted columnar aerosol single-scattering albedo to within 0.01 when a non-absorbing background aerosol is mixed with dust (Table B3). This latter point indicates the differences in near-forward scattering between the two aerosol models do not greatly affect the retrieved $\omega_0(\lambda)$. Hence, the effect of a background aerosol upon our retrievals may be accurately estimated using the retrieved $\omega_0(\lambda)$ and reasonable assumptions regarding the radiative properties of the background aerosol. We note this may not be the case when smaller aerosols with weaker near-forward scattering (e.g., biomass burning aerosol) are dominant, or a more strongly

absorbing aerosol is present. In this instance, however, even a non-absorbing ($\omega_0=1.00$) background aerosol has only a small influence on the retrieved single-scattering albedo (see Fig. B14).

4. Discussion

The single-scattering albedo and phase function of windblown African mineral dust have been retrieved with very low uncertainty from ground-based measurements of sky radiance with no assumptions of particle shape. The observed absorption is much less than mineral dust models that were constructed from laboratory measurements of Saharan aerosols on filter pads [Patterson, 1981]. These results suggest a weakly absorbing model of African dust is more appropriate for use in climate studies [Miller and Tegen, 1998; Myhre and Stordal, 2001; Perlwitz *et al.*, 2001], hence mineral dust cools Earth more than is generally believed. The retrieved single-scattering albedo agrees well with values obtained by different remote sensing methods near the African coast (Fig. B14), indicating $\omega_0(\lambda)$ of African dust does not change appreciably during transit of the Atlantic Ocean. This finding is in accord with indications that the mineralogy and size distribution of clay minerals are relatively stable beyond several hundred kilometers from the source [Glaccum and Prospero, 1980; Schütz *et al.*, 1981; Tegen and Lacis, 1996]. The disparity between the laboratory and remotely sensed values of ω_0 is interesting. Pure mineral dust should not absorb appreciably above $0.55\mu\text{m}$ [Gillespie and Lindberg, 1992; Sokolik and Toon, 1999], suggesting that black carbon, a frequent component of desert aerosols [Hansen *et al.*, 1993; Levin *et al.*, 1980], may have been present in the laboratory samples. Alternatively, haematite, a naturally occurring iron oxide that absorbs strongly in the visible and near-infrared [Sokolik and Toon, 1999], could have been present in significantly greater quantities in the dust samples.

The Wang-Gordon algorithm derives the columnar aerosol single-scattering albedo within 0.02 at visible wavelengths at optical depths as low as 0.3. AERONET retrievals are accurate to within 0.03 only

when aerosol optical depths are greater than 0.5 [Dubovik *et al.*, 2000]. Since mean aerosol optical depths of many species (e.g., Arabian and Asian mineral dust, biomass burning aerosols from south-west Africa) fall between 0.3 and 0.5 during peak seasonal activity [Husar *et al.*, 1997], successful AERONET retrievals require periods of unusually strong aerosol activity. The Wang-Gordon algorithm can thus serve as a valuable supplement to aerosol characterization studies, particularly during closure experiments for which success relies on obtaining an over-determined set of aerosol properties [Ogren, 1995; Sokolik *et al.*, 2001] within the allotted time period. The insensitivity of the algorithm to particle shape also promises to be useful in assessing the accuracy of nonspherical models used to deduce the optical properties of airborne mineral dust.

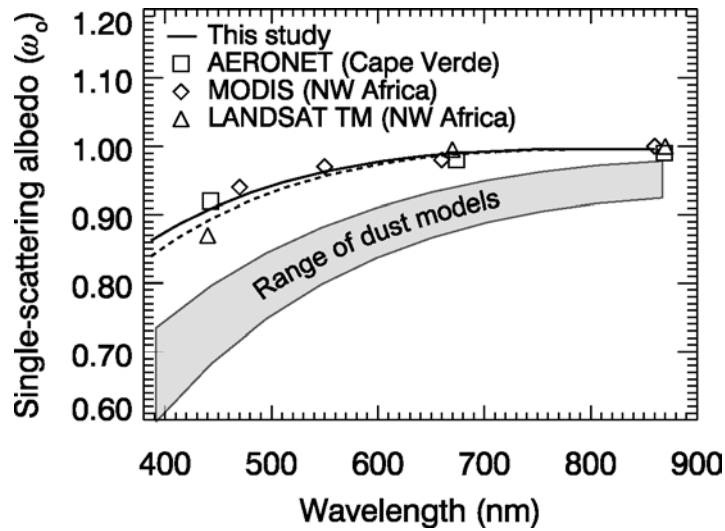


Figure B14. Comparison of retrieved single-scattering albedo from this study (solid line); as above but corrected for presence of background aerosol (dashed line; see text for details); AERONET [Holben *et al.*, 2001]; MODIS [Kaufman *et al.*, 2001]; and LANDSAT TM [Tanré *et al.*, 2001] with range of models constructed from laboratory measurements of imaginary refractive index of Saharan aerosol samples. Upper limit of dust models represents a long-range mineral dust model constructed using refractive index of Patterson [1977], geometric mean radius (r_g) of 0.5, natural logarithm of geometric standard deviation ($\ln\sigma_g$) of 0.79 [Schütz, 1980], lower limit represents interpolated values of Carlson and Caverly [1977] and Carlson and Benjamin [1980]. Results from d'Almeida [1987] fall between these values.

Acknowledgments.

The authors wish to thank Joe Prospero for kindly providing aerosol statistics for summer 1998, NOAA Air Resources Laboratory for use of their HYSPLIT back-trajectory code, NOAA Satellite Active Archive for providing AVHRR data to the public, Jeannette van den Bosch for help with the images, Michael Mischenko for making his T-matrix code available, and Yoram Kaufman and Oleg Dubovik for valuable discussion and suggestions. C. Catrall wishes to thank Robert Steward, in particular, for his assistance in the field. Much of this work was completed under the NASA Earth System Science Fellowship awarded to C. Catrall. The authors gratefully acknowledge financial support from NASA through contracts NAS 5-31716 (MODIS) and NAS 5-97137 (SIMBIOS Project) awarded to K. Carder and contract NAS5-31363 (MODIS) awarded to H.R. Gordon.